

LOWER LIMITS ON THE ANISOTROPY OF THE EXTRAGALACTIC GAMMA-RAY BACKGROUND IMPLIED BY THE 2FGL AND 1FHL CATALOGS

AVERY E. BRODERICK^{1,2}, CHRISTOPH PFROMMER³, EWALD PUCHWEIN³, PHILIP CHANG⁴, AND KENDRICK M. SMITH¹

¹ Perimeter Institute for Theoretical Physics, 31 Caroline Street North, Waterloo, ON, N2L 2Y5, Canada

² Department of Physics and Astronomy, University of Waterloo, 200 University Avenue West, Waterloo, ON, N2L 3G1, Canada

³ Heidelberg Institute for Theoretical Studies, Schloss-Wolfsbrunnengasse 35, D-69118 Heidelberg, Germany

⁴ Department of Physics, University of Wisconsin-Milwaukee, 1900 E. Kenwood Boulevard, Milwaukee, WI 53211, USA

Draft version April 4, 2024

ABSTRACT

In principle, the angular anisotropy in the extragalactic gamma-ray background (EGRB) places severe constraints upon putative populations of unresolved gamma-ray point sources. Existing estimates of the EGRB anisotropy have been constructed by excising known point sources, e.g., taken from the First or 2 Year *Fermi*-LAT Source Catalog (1FGL or 2FGL, respectively) and statistically analyzing the residual gamma-ray sky maps. We perform an independent check of the EGRB anisotropy limits by comparing the values obtained from the 1FGL-masked sky maps to the signal implied by sources that lie below the 1FGL detection threshold in the more sensitive 2FGL and 1FHL (First *Fermi*-LAT catalog of > 10 GeV sources). As such, our analysis provides an internal consistency check of implications for source counts and spectral index distributions of gamma-ray bright active galactic nuclei obtained from *Fermi*-LAT data. Based on this, we find evidence for substantially larger anisotropies than those previously reported at energies above 5 GeV, where BL Lac objects are likely to provide the bulk of their contribution to the EGRB. This uncertainty in the EGRB anisotropy cautions against using it as an independent constraint for the high-redshift gamma-ray universe. Moreover, this would suggest that contrary to previous claims, smooth extensions of the resolved point-source population may be able to simultaneously explain both the isotropic and anisotropic components of the EGRB.

Subject headings: BL Lacertae objects: general – gamma rays: general – radiation mechanisms: non-thermal

1. INTRODUCTION

The Large Area Telescope (LAT) on board the *Fermi* space telescope has proven to be a powerful tool for studying the extragalactic component of the gamma-ray sky. It has already detected more than 1800 discrete point sources, the overwhelming majority of which is associated with active galactic nuclei (AGNs; specifically blazars), with small populations of dimmer, though potentially much more numerous, sources (e.g., starburst and radio galaxies, see Table 6 of Nolan et al. 2012). These observations have produced the strongest constraints to date upon the gamma-ray bright blazar population and its evolution.

Likewise, the unresolved component of the extragalactic gamma-ray sky constrains the nature and number of point sources that lie below the current detection threshold. At present this arises in two contexts: (1) the isotropic extragalactic gamma-ray background (EGRB) spectrum, which sets the total flux that must be accounted for, and (2) the angular structure in the EGRB, characterized by an anisotropy coefficient (see below), that limits the fraction of the EGRB that can be produced by bright point sources. Of these, the second has the most severely constrained models that produce the EGRB from extensions of the gamma-ray point-source populations to low fluxes and high redshifts.

Attempts to model the EGRB by extending existing point-source populations receive strong theoretical support from our current understanding of the history of baryon accretion into dark matter halos and its associated observational tracers. Such models have been generally successful in reproducing the observed EGRB brightness and energy spectrum, both via phenomenological and physically motivated extensions (see, e.g., Singal et al. 2012; Broderick et al. 2012, 2014; Cavadini et al.

2011). They also receive qualitative support from the structure of the measured EGRB angular power spectrum, C_ℓ , within a variety of energy bands. Between $\ell = 150$ and 500, the C_ℓ are constant, consistent with the EGRB being produced by a population of discrete sources with angular scales smaller than the width of the *Fermi* point-spread function (PSF; Ackermann et al. 2012a).

Quantitatively, however, the EGRB power spectrum is *not* consistent with point-source populations that are extensions of the known gamma-ray bright source populations. Studies that have purported to show such agreement have done so accounting for only a subset of the known point-source population (see, e.g., Cuoco et al. 2012; Harding & Abazajian 2012). The origin of the limit is easy to understand: if the EGRB is produced by a few sources just below the current detection thresholds, it should exhibit a correspondingly large degree of angular variability. From this, it has been argued that no more than 20% of the isotropic EGRB can be due to gamma-ray blazars without violating the EGRB anisotropy constraints, and thus motivated renewed interest in alternative gamma-ray sources (Cuoco et al. 2012). However, this conclusion is predicated upon the proper normalization of the angular power.

This normalization remains uncertain for at least two reasons. First, it is necessary to deconvolve the *Fermi*-LAT PSF from the observed EGRB power spectrum to obtain the desired intrinsic spectrum, from which the EGRB anisotropy is determined. As a result, any errors in the assumed PSF will inevitably generate corresponding errors in the anisotropy normalization. Second, the uncertainty estimates were based upon expressions that assumed the background is well approximated by a Gaussian random field. While these are appropriate for large populations of intrinsically weak sources, they are misleading when the EGRB anisotropy is dominated by a handful

of point sources near the detection threshold. In the latter case, the observed gamma rays are strongly correlated via the nature of their origin, resulting in a substantially larger EGRB anisotropy uncertainty.

In addition, the general success of extensions of the known blazar population to low fluxes provides a natural reason to revisit the EGRB anisotropy normalization. However, more disturbing is the precipitous decline in blazar numbers below the *Fermi* detection threshold required for consistency. This is difficult to envision, even in principle, requiring a pathological redshift evolution and luminosity function for which there is currently no other evidence (Harding & Abazajian 2012, see also Section 4.2 of the present work). Most disconcerting, this would represent an obstacle to unifying the gamma-ray blazar population with that of other AGNs, would be at odds with the underlying physical picture of accreting black hole systems, and would suggest a conspiracy between accretion physics and the formation of structure. By analogy with Galactic X-ray binaries, in the unified picture of AGNs, these systems are thought to switch between their accretion states, cycling between the high/soft state (i.e., quasars) and the low/hard state (i.e., radio-loud AGNs) on the dynamical timescale of the inner accretion flow, instead of those associated with the supply of available gas (Maccarone et al. 2003; McHardy et al. 2006). This picture would predict that AGN types associated with the various accretion states to have contemporaneous populations. This receives indirect support from the apparent rapid redshift evolution of radio-loud AGNs, the presumed parent population of blazars, which peak near $z \sim 1.85$ (Willott et al. 2001; Wall et al. 2005).

Motivated by this, here we present an external, empirical assessment of the normalization of the reported EGRB anisotropy. We do this by exploiting the sensitivity difference between the First and 2 Year *Fermi*-LAT Source Catalogs (1FGL and 2FGL, respectively, Abdo et al. 2010a; Nolan et al. 2012) and the more recently published First *Fermi*-LAT catalog of > 10 GeV sources (1FHL, Ackermann et al. 2013). The EGRB anisotropy measurements reported by Ackermann et al. (2012a) employed the 1FGL for point-source identification and removal. Despite this, the *Fermi* data used for the anisotropy measurement were collected over a 22 month period, coincident with the 24 month period used to construct the more sensitive 2FGL and 36 month period used to construct the 1FHL. Thus, subsets of the 2FGL and 1FHL will have contributed to the observed EGRB anisotropy calculated from sky maps where 1FGL point sources have been masked. By comparing their contributions to the observed EGRB anisotropy with the reported values, we obtain independent limits on the EGRB anisotropy magnitude.

Note that this is quite different than the discussion of the dependence upon the catalog (1FGL or 2FGL) used to construct the point-source mask in Ackermann et al. (2012a). There the fraction of the EGRB anisotropy associated with the 2FGL was assessed by comparing the anisotropy signal in residual sky maps obtained by masking on the 2FGL sources instead of the 1FGL (which comprised their main analysis). Here, we are concerned with verifying the absolute normalization of the anisotropy signal using an *independent* and potentially more robust method that is based directly on the properties of the unmasked point sources listed in the 2FGL and 1FHL rather than on the angular power spectra of the residual sky maps.

In the interests of completeness, we present a variety of estimates of the expected anisotropy. These may be broadly placed into two categories: estimates that explicitly use the sources in

the 2FGL and 1FHL that are unmasked by the 1FGL (which we call “direct estimates”) and estimates that use the entire 2FGL and 1FHL as statistical measures of the unmasked source population (“statistical estimates”). The former set is much more susceptible to cosmic variance, though places hard lower limits on the measured EGRB anisotropy spectrum. In practice, these are almost certainly substantial underestimates, as they are predicated upon the physically unreasonable assumption that sources below the band-specific detection threshold contribute nothing. The statistical estimates are likely more robust as a result of the considerably larger statistical sample from which they are drawn. Perhaps more importantly, they are more directly relevant for comparison to theoretically motivated source populations, which typically assume isotropy, and are thus insensitive to the potentially large cosmic variance associated with the considerably smaller masked population. The assumption made is that an accurate statistical description of the sources that remain after masking on the 1FGL can be obtained from the 2FGL source population (which we will justify empirically). In all cases, we find qualitatively similar results: in the absence of a pathological decline in high-energy gamma-ray flux in sources just below the *Fermi* detection threshold at high energies, the reported EGRB anisotropy calculated from masking the 1FGL point sources is significantly below what may be already accounted for from the observed point-source populations in the 2FGL and 1FHL. A summary of the lower limits upon the anisotropy within the energy bands reported in Ackermann et al. (2012a) is collected in Table 1, together with a brief description of the method employed and the section where it is described.

We begin in Section 2 with a short derivation of the contribution to the EGRB anisotropy spectrum from a population of point sources and a description of how we construct the relevant fluxes for each band. We present direct estimates for various subpopulations of the 2FGL and 1FHL in Section 3. Statistical estimates are collected in Section 4. In Section 5, we discuss our results in the context of the measured EGRB and possible reasons for differences. Finally, conclusions are collected in Section 6.

2. CONSTRUCTING ANISOTROPY POWER SPECTRA

2.1. Definition of C_P

Above $\ell \simeq 150$, the EGRB angular power spectrum is well characterized by a constant, i.e., $C_\ell = C_P$ (Ackermann et al. 2012a). In the flat-sky limit,¹ this is related to the gamma-ray flux map via

$$C_\ell = \int d^2\theta e^{i\ell \cdot \theta} \int \frac{d^2\theta'}{4\pi} \mathcal{F}(\theta' + \theta) \mathcal{F}(\theta'), \quad (1)$$

where for a given ensemble of unresolved point sources with fluxes $\{\mathcal{F}_j\}$ and positions θ_j the flux per unit solid angle is

$$\mathcal{F}(\theta) = \sum_j \mathcal{F}_j \delta^2(\theta - \theta_j). \quad (2)$$

¹ Expanding point-source sky maps obtained in Section 3 into spherical harmonics, we measure the angular power spectrum and verify that it becomes flat for multipoles $\ell > 15$ and consistent with a Poisson power spectrum. This provides an explicit validation of the flat-sky limit at multipoles of interest.

Table 1
Estimated Lower Limits upon the EGRB Anisotropy^a

Method ^b	Section	ΔC_P within various energy bands (10^{-19} ph 2 cm $^{-4}$ s $^{-2}$ sr $^{-1}$)			
		1.04–1.99 GeV	1.99–5.00 GeV	5.00–10.4 GeV	10.4–50 GeV
Ackermann et al. (2012a), DATA:CLEANED	—	46.2 ± 11.1	13.0 ± 2.2	0.85 ± 0.25	0.211 ± 0.086
Unmasked 2FGL detected in each energy band	3.1	27.5 ± 5.0	7.0 ± 1.3	0.63 ± 0.13	0.168 ± 0.063
Unmasked 1FHL detected above 10 GeV	3.1	—	—	—	0.238 ± 0.092
Unmasked 2FGL band-corrected \mathcal{F}_{35}	3.2	26.9 ± 3.7	8.6 ± 1.1	0.86 ± 0.11	0.54 ± 0.09
Statistical 2FGL, w/2FG	4.3	38.5 ± 2.8	12.5 ± 0.9	1.35 ± 0.11	0.98 ± 0.12
Statistical 2FGL, w/2FGL-EB	4.3	16.0 ± 2.7	5.2 ± 0.9	0.61 ± 0.11	0.52 ± 0.10
Statistical 2FGL, w/PL	4.3	49.8 ± 3.4	16.1 ± 1.0	1.71 ± 0.13	1.20 ± 0.13
Statistical 2FGL, w/PL-EB	4.3	36.7 ± 2.0	11.9 ± 0.6	1.29 ± 0.08	0.94 ± 0.10
Statistical 2FGL, hard sources w/2FGL	4.3	6.9 ± 0.9	4.1 ± 0.5	0.73 ± 0.09	0.76 ± 0.11
Statistical 2FGL, hard sources w/2FGL-EB	4.3	3.5 ± 0.7	2.1 ± 0.5	0.39 ± 0.09	0.45 ± 0.10
Statistical 2FGL, hard sources w/PL	4.3	8.9 ± 1.1	5.1 ± 0.6	0.90 ± 0.10	0.91 ± 0.13
Statistical 2FGL, hard sources w/PL-EB	4.3	7.0 ± 0.8	4.0 ± 0.4	0.71 ± 0.07	0.73 ± 0.10
Statistical power law extension w/ $\mathcal{F}_{35} > 3 \times 10^{-10}$ ph cm $^{-2}$ s $^{-1}$ and PL	4.4	84.9 ± 9.2	27.2 ± 2.8	2.80 ± 0.34	1.73 ± 0.30
Statistical power law extension w/ $\mathcal{F}_{35} > 3 \times 10^{-10}$ ph cm $^{-2}$ s $^{-1}$ and PL-EB	4.4	68.5 ± 5.9	21.9 ± 1.8	2.26 ± 0.22	1.40 ± 0.19
Statistical power law extension w/ $\mathcal{F}_{35} > 10^{-10}$ ph cm $^{-2}$ s $^{-1}$ and PL	4.4	145.0 ± 9.6	46.4 ± 3.0	4.78 ± 0.35	2.96 ± 0.31
Statistical power law extension w/ $\mathcal{F}_{35} > 10^{-10}$ ph cm $^{-2}$ s $^{-1}$ and PL-EB	4.4	128.6 ± 6.6	41.2 ± 2.0	4.24 ± 0.24	2.63 ± 0.21
Statistical power law extension w/ $\mathcal{F}_{35} > 10^{-12}$ ph cm $^{-2}$ s $^{-1}$ and PL	4.4	187.4 ± 9.6	60.0 ± 3.0	6.18 ± 0.35	3.83 ± 0.31
Statistical power law extension w/ $\mathcal{F}_{35} > 10^{-12}$ ph cm $^{-2}$ s $^{-1}$ and PL-EB	4.4	171.1 ± 6.6	54.8 ± 2.0	5.64 ± 0.24	3.50 ± 0.22

^a The 1σ uncertainty intervals indicate the cosmic variance and include the propagation of flux uncertainties.

^b See Table 3 for the definitions of the threshold functions 2FGL, 2FGL-EB, PL, and PL-EB.

Inserting this into the above equation and averaging over ensembles (including source sky positions) yields

$$\begin{aligned}
 \langle C_\ell \rangle &= \left\langle \int d^2\theta e^{i\ell \cdot \theta} \int \frac{d^2\theta'}{4\pi} \sum_{j,k} \mathcal{F}_j \mathcal{F}_k \delta^2(\theta' + \theta - \theta_j) \delta^2(\theta' - \theta_k) \right\rangle \\
 &= \left\langle \sum_{j,k} \frac{\mathcal{F}_j \mathcal{F}_k}{4\pi} e^{i\ell \cdot (\theta_j - \theta_k)} \right\rangle \\
 &= \left\langle \sum_j \frac{\mathcal{F}_j^2}{4\pi} \right\rangle,
 \end{aligned} \tag{3}$$

where we identify the final expression with C_P . Note that larger individual fluxes or an enhanced number of sources increases this dimensional measure of the anisotropy coefficient C_P .

2.2. Relationship to Source Distributions

If the flux distribution of *unresolved* sources is a function of \mathcal{F} only, this reduces to the standard expression $C_P = \int d\mathcal{F} \mathcal{F}^2 d\mathcal{N}/d\mathcal{F}$, where $d\mathcal{N}/d\mathcal{F}$ is the number of sources *unresolved* in the 1FGL per steradian per unit flux. Generally, this can be quite complicated, with the result that

$$C_P = \int d^n p \mathcal{F}^2 \frac{d\mathcal{N}}{d^n p}, \tag{4}$$

where \mathbf{p} are some set of n parameters needed to describe the flux distribution (e.g., flux and spectral index, or in our case here, the 1–100 GeV band flux \mathcal{F}_{35} and spectral index). Further progress requires an explicit estimate for $d\mathcal{N}/d^n p$.

Here, we will use the 2FGL and 1FHL to provide an approximation of the source population that is (statistically) not detected in the 1FGL. We do this primarily via distributions of the form

$$\frac{d\mathcal{N}}{d\mathcal{F}d\Gamma} \simeq \sum_j \frac{w_j}{\Omega_{\text{sky}}} \delta(\mathcal{F} - \mathcal{F}_j) \delta(\Gamma - \Gamma_j), \tag{5}$$

where Ω_{sky} is the fraction of the sky being included, F_j are the band-specific fluxes, and the w_j are source-dependent weights describing the likelihood that a given source was not observed in the 1FGL². Effectively, in Equation (5), we are constructing the source distribution directly from the 2FGL, as opposed to utilizing fits to previously selected forms of $d\mathcal{N}/d\mathcal{F}d\Gamma$, as has been the case elsewhere (see, e.g., Cuoco et al. 2012). These empirical estimates of the source distribution correspond to conservative estimates of the lower limit on the EGRB anisotropy from unresolved blazars, with objects unresolved in the 2FGL further enhancing the anisotropy. For comparison, we also consider a simple extrapolation of the 2FGL $d\mathcal{N}/d\mathcal{F}d\Gamma$ to assess the fraction of the contribution to the EGRB anisotropy arising from sources in the 2FGL alone.

Inserting Equation (5) into the estimate for C_P , Equation (4), gives our conservative estimate of the 2FGL contribution to the measured EGRB anisotropy:

$$C_P = \frac{1}{\Omega_{\text{sky}}} \sum_j \mathcal{F}_j^2 w_j. \tag{6}$$

This procedure is then repeated for each energy band reported in Ackermann et al. (2012a), yielding a construction of the C_P spectrum.

2.3. Cosmic Variance Error Estimate

While a number of potential sources of uncertainty are present in principle, after the detection efficiency, chief among them is cosmic variance. We define this to be the statistical uncertainty associated with the choice of a particular realization of point sources from the given flux distribution, which remains even after the individual source parameters are fully characterized. Via a procedure similar to that employed above,

² Modulo the weights, w_j , this is simply the approximation of the probability distribution often used for bootstrap methods.

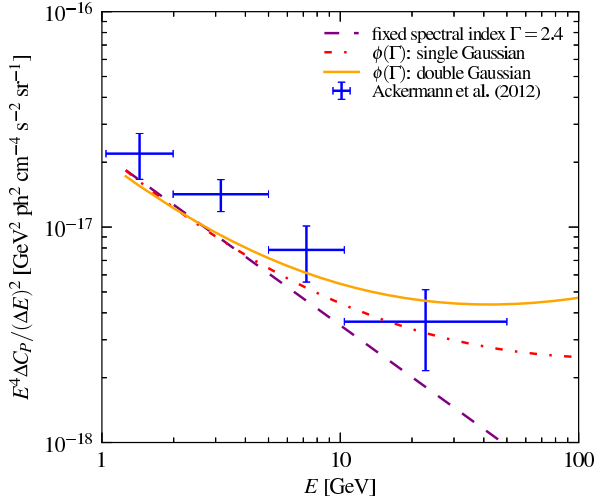


Figure 1. Reported EGRB anisotropy spectrum (blue error bars, taken from Ackermann et al. 2012a) in comparison to that implied by the flux distribution presented in Cuoco et al. (2012) for various choices of the photon spectral index distribution. Shown in black is the model presented in Cuoco et al. (2012), in which the photon spectral index is fixed at the average value for blazars; in red, a single-Gaussian model based upon the total blazar population from Abdo et al. (2010b); in purple, a double-Gaussian model based upon separate FSRQ and BL Lac populations. As the hard population is modeled with increasing accuracy, the anisotropy at high energies rises substantially, inducing a typically concave shape. Note that the Cuoco et al. (2012) flux distribution underestimates the total number of 2FGL sources near the flux threshold by roughly a factor of two.

we estimate this to be

$$\sigma_{C_P} = C_P \frac{\sqrt{\sum_j \mathcal{F}_j^4 w_j}}{\sum_j \mathcal{F}_j^2 w_j}. \quad (7)$$

Typical values of σ_{C_P}/C_P are 6%–10%. By comparison, the error induced by the intrinsic uncertainty in the band-corrected flux, ignoring any uncertainty associated with the spectral shape correction (see Appendix A.2), is estimated to be roughly 2%–7% (see Appendix B.1). Where relevant, both are included in the error estimates shown. Note that because the 2FGL contribution to the EGRB anisotropy is constructed directly from the point sources, there is no photon noise term (beyond that associated with the point-source flux uncertainties themselves).

To make further progress, we must describe how the weights, w_j , are determined and how estimates for the band-specific fluxes, \mathcal{F}_j , are obtained. The remainder of this section describes how the band-specific fluxes are obtained. We defer a full discussion of the weights until the presentation of the direct (Section 3) and statistical (Section 4) approaches to the construction of the source distribution.

2.4. Critical Importance of Spectral Information

Suggested by the choice of parametrization in the previous section, the distribution with respect to the spectral shape is critical to accurately estimating C_P . While this is briefly alluded to in Cuoco et al. (2012), here we emphasize this point. That is, power-law anisotropy spectra are a result of pathological photon spectral index distributions and are generally *not* expected. Commonly, the paucity of hard sources combined with their increasing dominance of the background at high energies results in a characteristic concave anisotropy spectrum, with potentially large enhancements above 10 GeV. While some spectral softening does occur above 30 GeV (see Appendix

A.2), potentially leading to a decrease in C_P at high energies, reproducing a power-law anisotropy spectrum requires an unlikely conspiracy between the spectral index distribution at low energies and the softening at high energies.

Figure 1 shows the anisotropy spectrum obtained for the flux distribution employed in Cuoco et al. (2012) for various spectral index distributions.³ Effectively, these modify the band correction that is used to relate the anisotropy at different energy bands. For a single power-law spectrum, the photon flux between energies E_m and E_M is related to the photon flux between E_x and E_y via a band correction, i.e.,

$$\mathcal{F}_{mM,j} = K(\Gamma_j) \mathcal{F}_{xy,j} \quad \text{where} \quad K(\Gamma) \equiv \frac{E_m^{1-\Gamma} - E_M^{1-\Gamma}}{E_x^{1-\Gamma} - E_y^{1-\Gamma}}. \quad (8)$$

In the limit that $E_M - E_m \ll E_m, E_M$, the band correction becomes

$$K(\Gamma, E) \equiv (1 - \Gamma) \Delta E \frac{E^{-\Gamma}}{E_x^{1-\Gamma} - E_y^{1-\Gamma}}, \quad (9)$$

in terms of which

$$C_P(E) = C_{P,xy} \int d\Gamma K(\Gamma, E)^2 \phi(\Gamma), \quad (10)$$

where $\phi(\Gamma)$ is the normalized photon spectral index distribution.

In their anisotropy estimates, Cuoco et al. (2012) assumed a fixed value of $\Gamma = 2.40$, corresponding to $\phi(\Gamma) = \delta(\Gamma - 2.40)$. This is shown by the purple long-dashed line in Figure 1 for the flux distribution employed there. However, in practice, this almost certainly significantly underestimates the anisotropy at high energies, which is dominated by the subset of hard sources. This is evident by the remaining lines, differing only in their choice of the spectral index distribution.

In particular, in Figure 1, we also show models with $\phi(\Gamma)$ given by a single Gaussian and a double Gaussian with equal weights, meant to reproduce the intrinsic spectral distributions found for all blazars and for the FSRQs and BL Lac objects separately by Abdo et al. (2010b).⁴ In the single-Gaussian model the mean and standard deviation are 2.4 and 0.24, respectively, which is sufficient to substantially bend the anisotropy spectrum upward at high energies. This is even more explicit for the double-Gaussian model, which models the softer FSRQs (mean 2.47 and std. dev. 0.19) and harder BL Lac objects (mean 2.20 and std. dev. 0.22) separately. Since this increases the low- Γ wing, it further enhances the high-energy anisotropy.

While a seemingly minor distinction, it is clear from Equation (10) that it is the mean K^2 that enters into the definition of $C_P(E)$, not the mean Γ or mean K . Nevertheless, this has significant implications where the source population is dominated by a small number of objects. For these reasons, we take special care to ensure that the impact of the spectral distribution is accounted for via variations upon Equation (5). Because of this, in all of the anisotropy spectra presented here, the associated concave behavior is readily apparent as anticipated.

³ Note that the fitted 1LAC flux distribution Cuoco et al. (2012) employed is shown in comparison to the observed 2FGL flux distribution in Figure 7, and underpredicts the number of sources by roughly a factor of two near the detection threshold. We consider it here for comparison only.

⁴ We use the 1LAC sample properties here for consistency with Cuoco et al. (2012).

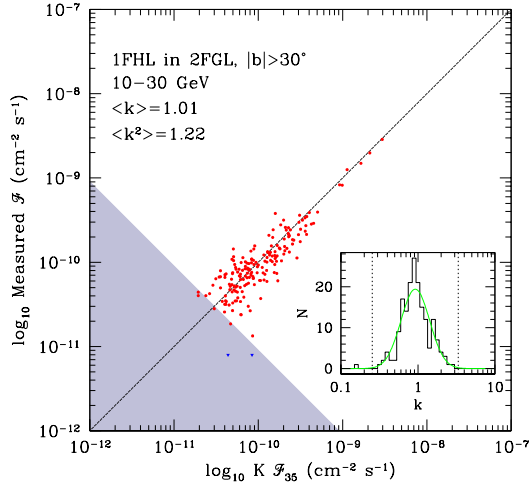


Figure 2. Comparison of the 10 GeV–30 GeV flux reported in the 1FHL and obtained by a band correction from the 1 GeV–100 GeV 2FGL flux (assuming power-law spectra) for sources that appear in both catalogs. Measured fluxes are shown by the red squares; upper limits are shown by the blue triangles. The detection threshold is denoted by the grayed region in the lower left. For reference, the dotted line shows equality. Spectral softening, which we ultimately account for via the spectral shape correction, k_{mM} , is responsible for the offset between the observed fluxes and those obtained by the band correction alone. Shown in the inset is the distribution of the spectral shape correction. See Appendix A.2 for more detail regarding how this is derived and the average values constructed. (Note that while all sources in the 1FHL are detected above 10 GeV, not all 1FHL sources are detected in the specific 10 GeV–30 GeV band shown here.)

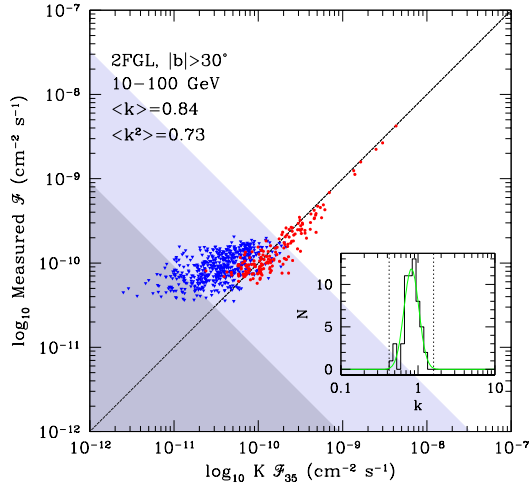


Figure 3. Comparison of the 10 GeV–100 GeV flux reported in the 2FGL and obtained by a band correction from the 1 GeV–100 GeV 2FGL flux (assuming power-law spectra). Measured fluxes are shown by the red squares; upper limits are shown by the blue triangles. The 2FGL and 1FHL detection thresholds are denoted by the light and dark gray regions in the lower left, respectively. For reference, the dotted line shows equality. Spectral softening, which we ultimately account for via the spectral shape correction, k_{mM} , is responsible for the offset between the observed fluxes and those obtained by the band correction alone. Shown in the inset is the distribution of the spectral shape correction. See Appendix A.2 for more detail regarding how this is derived and the average values are constructed.

2.5. Summary of Band Correction and the Impact of Spectral Softening

Table 2
Spectral Corrections to the band-correction for *Fermi* Point Sources.

E_m^a	E_M^a	F_{\min}^b	$\langle k \rangle$	$\langle k^2 \rangle$
0.3	1	2×10^{-9}	1.01	1.05
1	3	5×10^{-10}	1.06	1.16
3	10	1.5×10^{-10}	1.04	1.13
10	30	3×10^{-11}	1.01	1.22
30	100	2×10^{-11}	0.88	1.08
100	500	2×10^{-11}	0.47	0.29

^a In units of GeV

^b In units of $\text{cm}^{-2}\text{s}^{-1}$

Where sources are detected within the particular energy bands in which the anisotropy has been reported, no band correction is needed. However, it is typically the case that source fluxes either are reported only in nearby energy ranges or are not detected at all at high energies. For these cases, some band correction is required. We describe this process in detail in Appendix A.2, and thus summarize the salient points here.

In the former case, when the source is detected at high energies in adjacent energy bands, we simply apply the power-law band correction in Equation (8). The error from this procedure is expected to be small because of the small extrapolation involved.

Nevertheless, when the source is detected only at low energies, the applicability of the power-law band correction is not immediately obvious. We address that here by comparing the power-law band-corrected 1 GeV–100 GeV fluxes to measured sub-band fluxes for sources within the 2FGL and sources that appear in both the 2FGL and 1FHL (the latter case providing better energy resolution above 10 GeV). Examples may be found in Figures 2 and 3, as well as in Appendix A.2. Note that we apply a condition solely upon the photon flux from 1 to 100 GeV (\mathcal{F}_{35}) since there is no systematic correlation between \mathcal{F}_{35} and the photon spectral index, Γ (see Section 4.2 and Cuoco et al. 2012).

Below 30 GeV, the power-law band-corrected fluxes provide an excellent fit to the measured fluxes. At higher energies, the relationship remains linear, with a constant of proportionality that decreases with the energy band, indicating the presence of spectral softening (which becomes substantial above 100 GeV). For this reason, we define a spectral shape correction factor

$$k_{mM} \equiv \frac{\mathcal{F}_{mM}}{K\mathcal{F}_{35}}. \quad (11)$$

Within each energy band, the k_{mM} appear well characterized by a log-normal distribution, with a width that is independent of source flux and increases with gamma-ray energy. We therefore assume that the k_{mM} are log-normal random variables, in terms of which the reconstructed flux is $\mathcal{F}_{mM} = k_{mM}K\mathcal{F}_{35}$. The mean k_{mM} , $\langle k \rangle$, are listed in Table 2 and are comparable to unity below 30 GeV, falling to 0.88 for 30 GeV–100 GeV, and dropping rapidly thereafter, presumably due to photon attenuation off of the optical/UV background (Ackermann et al. 2012c; Domínguez et al. 2013).

There does not appear to be any evolution of k_{mM} with source flux, and thus dimmer sources appear to exhibit the same shape correction as brighter objects. Nevertheless, by its definition, the 1FHL includes only sources that have been detected above 10 GeV, and thus it is not immediately obvious that for sources below the detection threshold that this remains true. Figure 3 shows the same analysis for all power-law objects within

the 2FGL (the class of sources we will employ henceforth, by virtue of the applicability of the power-law band correction). In this case, there are many upper limits associated with non-detections (denoted by the blue triangles in Figure 3). These form a plateau at higher measured fluxes than our band-corrected value. Thus, there is at present no evidence for a flux-dependent softening at or just below the detection threshold.

It is important at this stage to note that $\langle k \rangle$ is *not* what matters for the definition of the C_P . Rather, since it is the square of the flux that enters, it is the square of the spectral shape correction, and thus since there is no apparent correlation between the spectral shape and flux, $\langle k^2 \rangle$. By definition, this is larger than $\langle k \rangle^2$, and even for the 30 GeV–100 GeV band greater than unity. That is, the contributions from the highest flux sources will dominate the anisotropy spectrum, resulting in a moderation in the impact of a decreasing mean flux when the scatter in the distribution rises. Thus, below 100 GeV, spectral softening typically makes $\lesssim 10\%$ correction to the band-corrected fluxes of individual sources and $\lesssim 15\%$ enhancement in their contributions to the anisotropy.

In the following, we present anisotropy power spectra for different energy bands that have been “band corrected” in two steps. (1) Considering only sources that are well fit by a power-law spectrum, we make a gross band correction for each object and compute the resulting anisotropy power spectra C_P . (2) We correct each band power of C_P with our empirically found correction factor $\langle k^2 \rangle = 1.13$ for residual spectral curvature (see Appendix A.2), assuming this correction factor to be independent of source flux.

3. DIRECT ESTIMATES OF THE EGRB ANISOTROPY

The direct methods are characterized by how the w_j in Equation (5) are chosen: set either to zero or unity depending on whether or not the source in question would have been masked out via the procedure followed in Ackermann et al. (2012a).

We reproduce the mask employed by Ackermann et al. (2012a) by first excluding sources within 2° circular regions centered on all sources reported in the 1FGL and then by applying a Galactic latitude cut, e.g., $|b| > 30^\circ$. The resulting mask is shown in Figure 4. Unlike Ackermann et al. (2012a), since we are estimating the contribution from resolved point sources directly, we are not limited by the contaminating diffuse Galactic emission component. Thus, we are able to consider alternative Galactic latitude cuts, providing some measure of the role cosmic variance plays. Upon comparing the point-source populations at various potential Galactic latitude cuts, we find a strong similarity in the point-source populations for $|b| > 15^\circ$ (see Appendix B.2). Hence, in what follows, we show both the $|b| > 30^\circ$ mask employed by Ackermann et al. (2012a) as well as results associated with a somewhat conservative, but nonetheless more complete, $|b| > 20^\circ$ cut.

Following the implementation of the mask, the resulting value of C_P is then obtained directly from Equation (6), giving

$$\Delta C_P = \frac{1}{\Omega_{\text{sky}}} \sum_j \mathcal{F}_j^2, \quad (12)$$

where the sum extends over all unmasked sources and $\Omega_{\text{sky}} = 4\pi f_{\text{sky}}$. Values of the unmasked sky fraction, f_{sky} , are obtained explicitly via a Monte Carlo integration of the respective sky masks (see Appendix B.2). Note that this is necessarily a

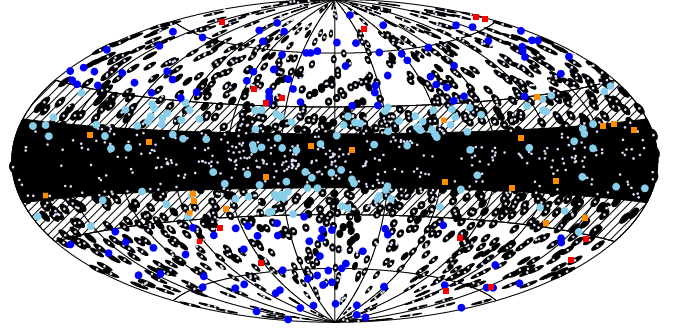


Figure 4. Aitoff projection of the 1FGL sky mask employed (black region). The low Galactic-latitude region ($|b| \leq 30^\circ$) is shown by the hatched area and the Galactic plane ($|b| \leq 15^\circ$) is shown in back. Masked 2FGL sources are shown by the gray dots. Unmasked 2FGL sources detected above 10 GeV are denoted by red (orange) squares at high (low) latitudes. Unmasked 2FGL sources with only upper limits in the 2FGL above 10 GeV are denoted by blue (light blue) circles at high (low) latitudes.

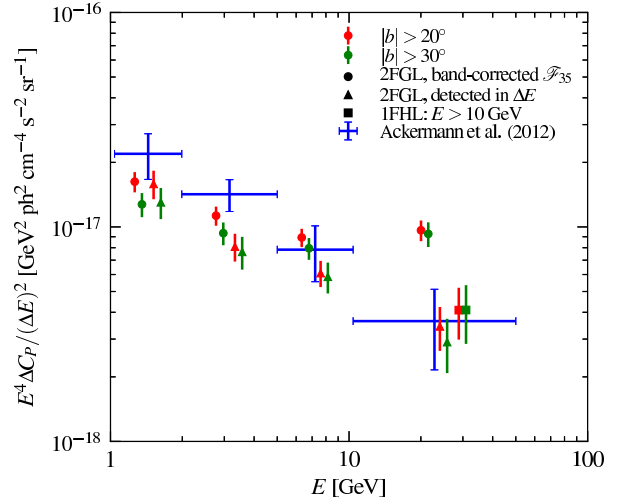


Figure 5. Contribution to the EGRB anisotropy ΔC_P by unmasked point sources employing two different latitude cuts of $|b| > 20^\circ$ (red) and $|b| > 30^\circ$ (green). We compare the reported measurements of C_P (blue, Ackermann et al. 2012a) to the contribution of individual unmasked 2FGL sources, which are detected in the respective energy bins (triangles) and the unmasked 1FHL sources above 10 GeV (squares). The contribution of all unmasked 2FGL sources (detected above 1 GeV) that are band corrected to the respective energy band (circles) already overproduce the *Fermi* measurement by 3.2σ (3.4σ) in the highest energy band for $|b| > 30^\circ$ ($|b| > 20^\circ$). The error bars indicate the cosmic variance and include the propagation of flux uncertainties. The points have been shifted horizontally within their respective energy bin centers for clarity.

lower limit; it both fails to include any potential diffuse component and the contributions from sources below the 2FGL/1FHL detection thresholds. For this reason, we denote the EGRB anisotropy spectrum estimates obtained here by ΔC_P , with the understanding that they can represent only a fraction of the total values.

Here we describe a variety of limits of the form described above, distinguished by the point-source catalog (2FGL and 1FHL) and estimate of the fluxes, \mathcal{F}_j , used.

3.1. C_P from Unmasked Sources with Detections in each Energy Band

In our most conservative approach, we *only* use sources with detections in the respective energy bands. Since the energy

bands reported in the catalogs do not correspond to the energy band of the reported C_P , the flux computation requires some spectral correction, which depends upon the spectral shape. Here, we only use those point sources that are well fit by a power-law spectrum with spectral index Γ (and are classified as such in the catalogs), making the standard band correction for each source individually, using Equation (8) to relate the fluxes in the target band ($E_{m,M}$) and the lower and upper energy limits of the bands reported in the catalogs ($E_{x,y}$). We apply the following band corrections to 2FGL sources.

$$\begin{aligned} 1-3 \text{ GeV} &\rightarrow 1.04-1.99 \text{ GeV, for 1-3 GeV sources,} \\ 1-10 \text{ GeV} &\rightarrow 1.99-5 \text{ GeV, for 3-10 GeV sources,} \\ 3-10 \text{ GeV} &\rightarrow 5-10.4 \text{ GeV, for 3-10 GeV sources,} \\ 10-100 \text{ GeV} &\rightarrow 10.4-50 \text{ GeV, for 10-100 GeV sources.} \end{aligned}$$

In the case of the 1FHL catalog, we band correct the 10–30 GeV fluxes to 10.4–50 GeV. As a result, we find 15 (21) unmasked sources for $|b| > 30^\circ$ in the highest-energy band of the 2FGL catalog (respectively the 10–30 GeV band of the 1FHL catalog) that contribute to ΔC_P . As shown in Figure 5, in the case of the 1FHL catalog, these 21 sources already explain the measured anisotropy in the high-energy band.

Note that this can only be a lower limit to the true anisotropy since in addition to the restrictions mentioned at the end of the preceding section, here it is further assumed that sources detected at lower energies in the 2FGL—which are not significantly detected at the high-energy band due to the decreasing *Fermi*-LAT sensitivity there—would not emit any flux at $E > 10$ GeV. This latter assumption is even more severe than assuming that the 2FGL is complete.

3.2. C_P from all Unmasked 2FGL Sources

Within the 2FGL, we find 139 unmasked power-law sources with $|b| > 30^\circ$, many more than the 15 that have explicit detections above 10 GeV. While possible, we consider it extraordinarily unnatural to believe that sources lying just below the high-energy *Fermi* detection threshold are completely devoid of high-energy gamma-ray emission, if only because these sources appear in all other ways to form a continuous distribution with those that have been detected. Thus, in principle, all of these should contribute to the ΔC_P . Here, we assess the point-source contribution to the EGRB anisotropy spectrum using fluxes band corrected from the 1–100 GeV band (\mathcal{F}_{35}) for all sources in the 2FGL. Note that this still assumes that the 2FGL is complete, and thus remains a *lower* limit on the expected ΔC_P .

In Figure 5, we show the contribution of all unmasked 2FGL power-law sources (i.e., detected above 1 GeV) that are band corrected to the respective energy band. At the highest-energy band, the inferred ΔC_P values exceed the *Fermi*-LAT measurement by 3.2σ (3.4σ) for $|b| > 30^\circ$ ($|b| > 20^\circ$). That is using only the unmasked 1FHL and 2FGL sources, the lower limit upon the anisotropy either fully accounts for, or significantly exceeds the reported values, respectively!

4. STATISTICAL ESTIMATES OF THE EGRB ANISOTROPY

The preceding direct estimates employed the realization of gamma-ray point sources present in the unmasked 2FGL/1FHL. However, both to reduce cosmic variance, which appears to produce an anomalously low anisotropy signal near latitude cuts of 30° (see Appendix B.2), and to provide a better comparison to theoretical models of the gamma-ray point-source population, we also provide a set of statistical estimates

of the EGRB anisotropy. These employ the entire 2FGL as a statistical representation of the point-source population. Key to this is the assumption of the isotropy (i.e., the masked and unmasked 2FGL sources are statistically similar) and a characterization of the 1FGL detection threshold, corresponding to the computation of the w_j in Equation (6). We treat both of these here before describing the corresponding estimate for the EGRB anisotropy spectrum.

4.1. Isotropy of the 2FGL

Clustering of the 2FGL sources would presumably decrease their representation in the sample after application of the mask. However, evidence for this isotropy may be found in the investigation of mask dependence in Ackermann et al. (2012a)⁵. Assuming Poisson statistics, with 154 more high-latitude sources ($|b| \geq 30^\circ$) found in the 2FGL than in the 1FGL, the anticipated ratio of unmasked sky fractions is

$$\frac{f_{\text{sky}}^{2\text{FGL}}}{f_{\text{sky}}^{1\text{FGL}}} \simeq e^{-(\Omega_{\text{psm}}/\Omega_b)\Delta N} = 0.910, \quad (13)$$

where $\Omega_{\text{psm}} = \pi(2^\circ)^2 = 3.83 \times 10^{-3}$ sr is the solid angle of the point-source mask and $\Omega_b(|b| \geq 30^\circ) = 2\pi$ is the solid angle residing above the Galactic latitude mask. This agrees nearly exactly with the stated ratio in Ackermann et al. (2012a), $0.295/0.325 = 0.907$, and our own estimate (see Appendix B.2), $0.310/0.338 = 0.917$, providing some confidence that clustering may be neglected. A more complete comparison of source properties with various latitude cuts is presented in Appendix B.2, where it was found that at Galactic latitudes above 15° the source populations are statistically similar (i.e., have similar flux and spectral properties) and have nearly identical numbers of point sources per unit solid angle at different Galactic latitudes (i.e., once the Galactic component no longer contributes significantly, the number of objects per square degree is fixed within the expected Poisson fluctuations).

4.2. The 1FGL Detection Threshold

In the direct measures, the 1FGL detection threshold entered implicitly through the mask. Here, we use the observed 1FGL source distribution to estimate the detection threshold explicitly and therefore assign explicit values to the w_j . In practice, this is consistent with a condition solely upon the photon flux from 1 to 100 GeV (\mathcal{F}_{35}). Importantly, there is no systematic correlation between \mathcal{F}_{35} and the photon spectral index, Γ (see the top panel of Figure 6 and Figure 1 of Cuoco et al. 2012). This is very different from the photon flux from 100 MeV to 100 GeV (\mathcal{F}_{25}), which strongly correlates with the photon spectral index for small fluxes due to the strong energy dependence of the point-spread function of *Fermi*-LAT below 1 GeV (see Appendix A of Abdo et al. 2010a; Cuoco et al. 2012). Hence, the intrinsic flux distribution function can either be directly studied above 1 GeV or by adopting a non-parametric method, which allows for reconstruction of it from the observationally biased flux distribution (Singal et al. 2012). In any case, the detection threshold is not, however, consistent with a simple cutoff, and in the interest of completeness, we characterize the threshold function here.

⁵ We do not appeal directly to the EGRB power spectrum since to do so we would beg the question, having assumed that the background is due nearly exclusively to point sources. Nonetheless, that we do find this to be the case, in retrospect, the EGRB power spectrum provides powerful confirmation of this assumption.

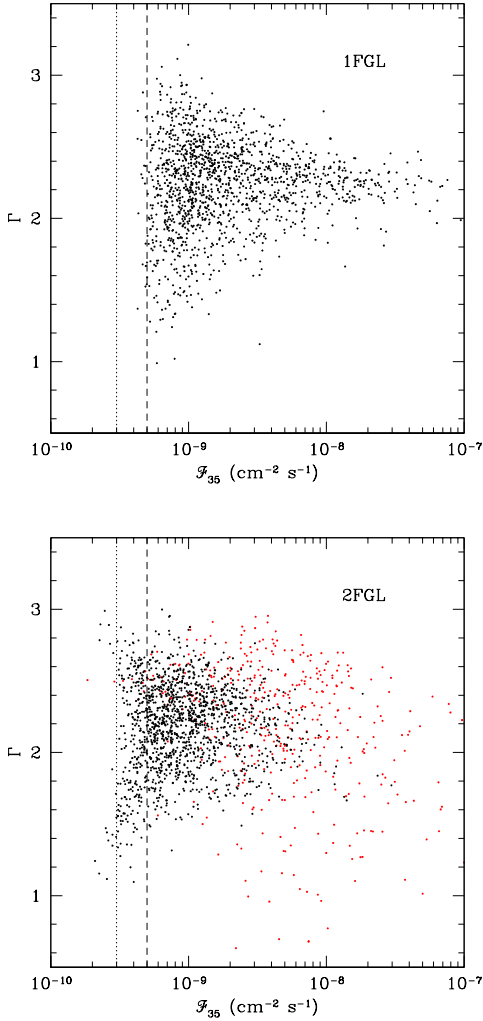


Figure 6. Photon spectral index vs flux for the 1FGL (top) and 2FGL (bottom). The vertical dotted lines show very roughly the flux limits of the 1FGL (dashed) and 2FGL (dotted). Red points in the latter indicate sources with spectra that are better fit with non-power-law models. These are excluded in the estimate of the EGRB anisotropy limits.

It is not possible to estimate the detection threshold from the 1FGL alone; as a result, some assumption must be made regarding the undetected source population. The flux distribution of the 1FGL is well approximated by a power law at high fluxes:

$$\frac{dN}{d\log_{10} \mathcal{F}_{35}} \simeq 1.8 \times 10^3 \left(\frac{\mathcal{F}_{35}}{10^{-9} \text{ ph cm}^{-2} \text{ s}^{-1}} \right)^{-1.25}, \quad (14)$$

(see Figure 7; note the above is corrected for sky fraction), providing a plausible upper bound upon the number of undetected sources.⁶ Also shown in Figures 6 and 7 is the 2FGL population. As anticipated, it extends to marginally lower fluxes, resolving a portion of the gamma-ray background unresolved by 1FGL, roughly consistent with the decrease expected from the increase in exposure time. At high fluxes, the normalized 1FGL and 2FGL are consistent with being drawn from the same population, i.e., above the 1FGL detection threshold,

⁶ The power law listed here differs from those reported in Abdo et al. (2010b) as a result of our using the 1 GeV–100 GeV fluxes.

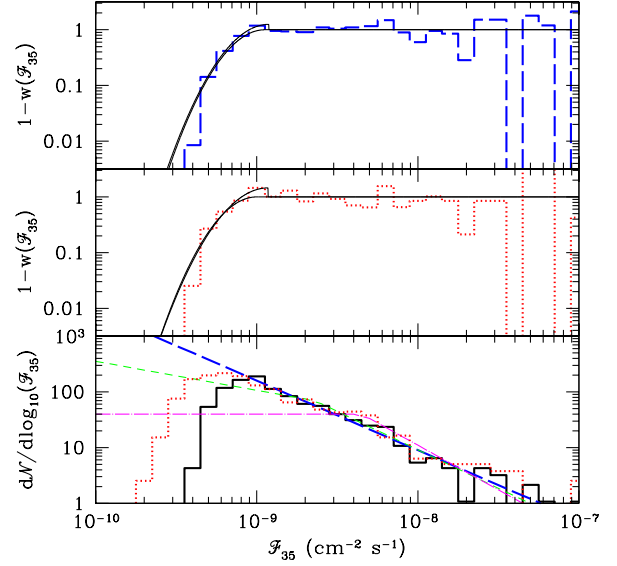


Figure 7. Bottom: distribution of 1FGL sources with 1 GeV–100 GeV flux (black), in comparison to two models for the true source distribution. At high fluxes, the distribution is well fit by a single power law (dashed blue line), which provides an upper limit upon the inferred source population at low fluxes. An absolute lower limit comes from the distribution of sources in the 2FGL, normalized to be consistent with the 1FGL for $\mathcal{F}_{35} > 10^{-9} \text{ ph cm}^{-2} \text{ s}^{-1}$ (dotted red line). In addition, for comparison we also show the flux distributions employed in Cuoco et al. (2012, dashed green line), and Harding & Abazajian (2012, dash-dot magenta line). Note that these are meant to reproduce the subpopulation of Fermi point sources corresponding to blazars. Middle and top: inferred detection efficiencies, $1-w(\mathcal{F}_{35})$, for the two approximations of the true source distribution shown in the bottom panel. In both cases, we show a best-fit non-negative $w(\mathcal{F}_{35})$ of the form described in the text and a version that allows $w(\mathcal{F}_{35})$ to extend below zero (detection efficiencies greater than unity) to describe the potential impact of Eddington bias upon the low-flux tail of the 1FGL source distribution. These bound the plausible range of detection efficiencies.

the source population flux distributions are statistically similar. Making the conservative assumption that the 2FGL is complete, it provides an absolute lower bound upon the number of undetected sources. More complicated source populations discussed in the literature fall between these two limits (see, e.g., Abdo et al. 2010b; Singal et al. 2012).

For comparison, the flux distributions employed previously by Cuoco et al. (2012) and Harding & Abazajian (2012) are also shown in Figure 7. We note that the subpopulation of gamma-ray sources comprised of blazars were being modeled in both cases. Nonetheless, it is clear that neither accurately reproduces the 1FGL or 2FGL source distribution, both exhibiting a break above the 1FGL flux threshold and substantially underestimating the number of gamma-ray sources immediately below it. This is a consequence of having been originally constructed in a different flux band, \mathcal{F}_{25} , for which the detection threshold exhibits a strong correlation with the source spectrum below $10^{-9} \text{ ph cm}^{-2} \text{ s}^{-1}$. Near this flux the observed flux distribution exhibits a break (Abdo et al. 2010b), though both its proximity to the flux at which detection threshold becomes independent of the photon spectral index and its absence in the \mathcal{F}_{35} flux distribution suggest that it is strongly impacted by the particular detection efficiency adopted. This is supported by the lack of any such feature in the 1FHL flux distribution after a careful debiasing near the flux threshold was performed (see, e.g., Figure 32 of Ackermann et al. 2013). Despite the critical differences at low fluxes, all estimates are similar at sufficiently

Table 3
Weight function Parameters for the 1FGL

Threshold Model	Source Distribution	\mathcal{F}_{\max}^a	m	y
2FGL	2FGL	1.00	7	0
2FGL-EB	2FGL w/Eddington bias	1.18	6	0.176
PL	Power law	1.12	7	0
PL-EB	Power law w/Eddington bias	1.19	6.5	0.097

^a Fluxes are in units of $(10^{-9} \text{ ph cm}^{-2} \text{ s}^{-1})$.

high fluxes, where the impact of the detection efficiency is minimal.

In practice, due to its abrupt nature, the detection threshold is only weakly sensitive to the form of the low-flux extension assumed. In both cases, it is well modeled by a log-normal cutoff. That is, the probability of *non-detection* is

$$w(\mathcal{F}_{35}) \simeq \begin{cases} 1 - 10^{-m[\log_{10}(\mathcal{F}_{35}/\mathcal{F}_{\max})]^2 + y} & \mathcal{F}_{35} < \mathcal{F}_{\max} \\ 0 & \text{otherwise,} \end{cases} \quad (15)$$

where the values of the various constants are listed in Table 3. The threshold flux, \mathcal{F}_{\max} , is consistently near $10^{-9} \text{ ph cm}^{-2} \text{ s}^{-1}$, and the steepness parameter, m , is near 6.5. While this consistently overpredicts the detection efficiency at very low fluxes, it provides a good approximation near the threshold and therefore at the fluxes that dominate the contribution to the EGRB anisotropy. The characteristic value of $5 \times 10^{-10} \text{ cm}^{-2} \text{ s}^{-1}$ employed by Cuoco et al. (2012) produces a similar threshold, if not slightly lower.

Some care should be taken in interpreting the distribution of sources near the detection threshold due to the potential for a significant Eddington bias (Eddington 1913, 1940). That this is present in the 1FGL is clear from the fact that the number of 1FGL sources right near the threshold *exceeds* that in the presumably more complete 2FGL. Deconvolving the Eddington bias is non-trivial and depends on both the instrumental and intrinsic fluctuations in the measured source fluxes. Here, we take a simplified, if somewhat unphysical approach, of allowing the detection efficiency to exceed unity immediately at the threshold, describing the detection of false positives corresponding to lower-flux sources that are temporally above the threshold due to statistical and intrinsic fluctuations (a similar approach is adopted in Ackermann et al. 2013, see Figure 30 and the surrounding discussion). This corresponds to a negative $w(\mathcal{F}_{35})$, and *lowers* the EGRB anisotropy.

Many bright sources, well above the putative 1FGL flux limit, appear in the 2FGL but not the 1FGL. Unlike the high-flux behavior, this is presumably due to variability, i.e., sources that were bright only following the initial nine months included in the 1FGL. Similarly, in the 2FGL, many 1FGL sources lie below the approximate 1FGL flux threshold, likely due to Eddington bias (both due to intrinsic variability and statistical fluctuations).

4.3. Estimating C_P from the 2FGL

We supplement the weights obtained above with a Galactic latitude cut of $|b| > 30^\circ$ to more directly represent the population of relevance to the results reported in Ackermann et al. (2012a). As previously mentioned, this guarantees that any Galactic point-source contribution has been eliminated. Inserting these conditions into Equation (6), i.e., only accounting for objects with $|b| > 30^\circ$ in the summation and employing the weights in Equation 15, then provides an estimate for the ΔC_P .

Note that in this case the source distribution is expressed in

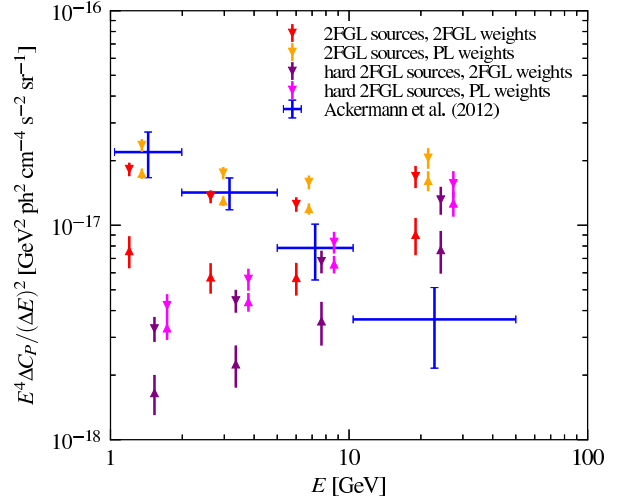


Figure 8. Reported EGRB anisotropy spectrum (blue error bars, taken from Ackermann et al. 2012a) in comparison to the implied contributions from high-latitude ($|b| > 30^\circ$) 2FGL sources (triangles). Downward pointing triangles assume the best-fit non-negative $w(\mathcal{F}_{35})$ of the form described in the text, and upward pointing triangles allow $w(\mathcal{F}_{35})$ to extend below zero (detection efficiencies greater than unity) to describe the potential impact of Eddington bias upon the low-flux tail of the 1FGL source distribution. Orange triangles show the EGRB anisotropy spectrum inferred assuming a power-law low-flux extension of the 1FGL, and the red triangles present the conservative lower limit obtained by assuming the 2FGL is complete. For reference, the contributions from only hard sources (i.e., $\Gamma \leq 2$) are also shown (purple and magenta). The error bars indicate the cosmic variance and include the propagation of flux uncertainties. The points are offset horizontally within their respective energy bin centers for clarity.

terms of \mathcal{F}_{35} and not the flux over the energy range for which C_P is being constructed, \mathcal{F} . This is necessary since our detection threshold is specified in terms \mathcal{F}_{35} ; fluxes over other energy ranges exhibit substantial spectral-index-induced biases. That is, we specify

$$\frac{d\mathcal{N}}{d\mathcal{F}_{35}d\Gamma} \simeq \sum_j \frac{w_j}{\Omega_{\text{sky}}} \delta(\mathcal{F}_{35} - \mathcal{F}_{35,j}) \delta(\Gamma - \Gamma_j), \quad (16)$$

where $w_j = w(\mathcal{F}_{35,j})$.

In accordance with the particular form of the band correction used and given the importance of the spectral shape to the reconstruction of the EGRB anisotropy, we restrict ourselves to the subset of the 2FGL that is best fit by power-law spectra, comprising roughly 78% of the total sample. Since the sources for which non-power-law fits are statistically favored tend to be bright, this restriction makes an insignificant difference in our EGRB anisotropy estimates in practice.

The estimated contribution to the EGRB anisotropy from the low-flux, high-latitude sources in the 2FGL is shown by the orange triangles in Figure 8, with the conservative lower limits arising from assuming the 2FGL is complete shown by the red triangles. The estimates using w_j that account for the Eddington bias in the 1FGL (upward pointing triangles for each method, respectively) are consistent with the direct estimates obtained in Section 3, yielding some confidence in the statistical approach. When w_j is constructed assuming a power-law extrapolation of the low-flux source population are used, the lower limits rise further.

Nevertheless, the anisotropy due to sources resolved by the 2FGL alone are sufficient to produce the entirety of the EGRB anisotropy from 2–5 GeV and *exceed* the reported EGRB anisotropy above 5 GeV by many σ . At high energies, this

is due primarily to the presence of hard gamma-ray sources, i.e., objects for which $\Gamma \leq 2$, shown by the magenta and purple triangles.⁷ These are dominated by BL Lac objects, and are presumably responsible for some fraction of the isotropic EGRB component. However, these are not solely responsible for the anisotropy excess, playing a subdominant role below 10.4 GeV.

4.4. Estimating C_P from Power-law Extensions of the 2FGL

The assumption made above that only sources that are detected in the 2FGL contribute to the EGRB anisotropy is itself extreme. While contributions to the C_P are heavily biased toward high-flux objects, the range about the flux threshold for which significant contributions are found extends for at least a decade. By comparison, the reduction in the detection threshold between the 1FGL and 2FGL is roughly 0.2 dex, considerably smaller. Thus, the assumption that the 2FGL is complete corresponds to a dramatic suppression in the number of sources immediately below the 2FGL detection threshold. Evidence that this is not the case may be found in the recently published catalog of hard Fermi sources, the 1FHL, which does not exhibit any notable features at the 2FGL flux limit. Hence, the ΔC_P obtained in the previous sections can at most represent a modest contribution to the anticipated value.

To provide a reasonable upper limit on the expected contribution to the EGRB anisotropy due to gamma-ray point sources, we consider the C_P obtained from a single power-law extrapolation of the 2FGL population, given in Equation (14). This is highly uncertain. To guarantee a finite contribution to the isotropic EGRB component, a break in the $dN/d\mathcal{F}_{35}$ relation must exist at sufficiently low fluxes. Similarly, to guarantee a finite source population, a cutoff must exist as well (though this is much less well constrained). To assess the sensitivity to these putative features, we produce anticipated EGRB anisotropy spectra for a variety of lower flux cutoffs.

We must supplement the extrapolated $dN/d\mathcal{F}_{35}$ relation with a spectral index distribution. Based on Figure 6, we assume the distribution in \mathcal{F}_{35} and Γ is separable, i.e., we choose

$$\frac{dN}{d\mathcal{F}_{35}d\Gamma} = \frac{dN}{d\mathcal{F}_{35}} \frac{e^{-(\Gamma-\bar{\Gamma})^2/2\sigma_\Gamma^2}}{\sqrt{2\pi}\sigma_\Gamma}, \quad (17)$$

where $\bar{\Gamma} = 2.2$ and $\sigma_\Gamma = 0.3$, measured from the 2FGL directly. While the intrinsic photon spectral index distribution is clearly skewed, the above does an especially good job of reproducing the hard component, critical for the high-energy EGRB anisotropy estimates.

Figure 9 shows the associated EGRB spectrum for a handful of lower-flux cutoffs. From this, it is apparent that the C_P receive a substantial contribution from sources that lie below the 2FGL flux threshold. In the absence of a dramatic suppression of the source population above $\mathcal{F}_{35} \simeq 10^{-10} \text{ cm}^{-2}\text{s}^{-1}$, these unresolved sources comprises more than half of the anticipated contribution.

5. DISCUSSION

While the direct estimate of the EGRB anisotropy above 10 GeV from the 1FHL is consistent with the reported values, this requires two extraordinary assumptions: first, that the 1FHL is complete, and second, that nearly all sources within

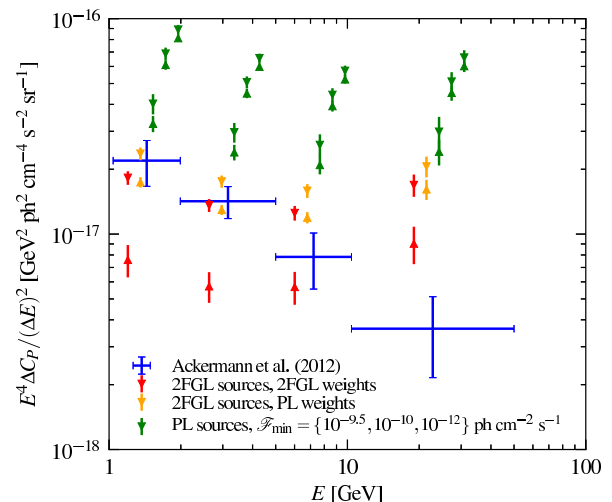


Figure 9. Reported EGRB anisotropy spectrum (blue error bars, taken from Ackermann et al. 2012a) in comparison to that inferred from a power-law extrapolation of the 2FGL to lower fluxes. The green triangles show the EGRB spectrum for various low-flux cutoffs, $3 \times 10^{-10} \text{ cm}^{-2}\text{s}^{-1}$, $10^{-10} \text{ cm}^{-2}\text{s}^{-1}$, and $10^{-12} \text{ cm}^{-2}\text{s}^{-1}$ (effectively zero) from left to right within each energy bin. Downward pointing triangles assume the best-fit non-negative $w(\mathcal{F}_{35})$ of the form described in the text, and upward pointing triangles allow $w(\mathcal{F}_{35})$ to extend below zero (detection efficiencies greater than unity) to describe the potential impact of Eddington bias upon the low-flux tail of the 1FGL source distribution. For reference, the red triangles show the limits obtained under the assumption that the 2FGL is complete (see Figure 8). The error bars indicate the cosmic variance and include the propagation of flux uncertainties. The points are offset horizontally within their respective energy bin centers for clarity.

the 2FGL that are undetected above 10 GeV have sufficiently softened spectra that they emit negligibly there. Excluding these, our lower limit upon the EGRB anisotropy spectrum significantly exceeds the values reported by Ackermann et al. (2012a). The reason for this is not immediately clear. Here, we consider a handful possibilities.

The first is that the 1FHL and 2FGL are complete and sources without detections above 10 GeV in the 2FGL and 1FHL really do have vanishing flux at that energy, i.e., band correcting their low-energy emission substantially overestimates their true high-energy fluxes. However, the former is belied by the absence of any feature near the flux thresholds of the 1FHL or 2FGL in the flux distributions. The latter is argued against by the detection of high-energy emission from a number of additional sources reported in the 1FHL, though presumably this may arise from variability. Perhaps more conclusive is the evidence that the spectrally corrected \mathcal{F}_{35} provides a good estimate of the 1FHL measured fluxes (see Appendix A.2), strongly suggesting that this will be true for sources falling immediately below the relevant detection thresholds. For this reason, we believe this is highly disfavored.

The second is that the deficit in anisotropy is due to a surfeit of dim sources in the 1FGL resulting from the Eddington bias. While we have not made any attempt to debias the 1FGL (which is well beyond the scope of this paper), this effect alone is incapable of producing the factor of two reduction necessary to resolve the discrepancy.

The third is the PSF deconvolution procedure employed by Ackermann et al. (2012a). The most recent PSF estimates are much broader than those used, implying a corresponding underestimate of the deconvolved C_P . As shown in Appendix C.1, rough estimates suggest that this can amount to a factor of

⁷ At all energies, however, the 2FGL contribution to the isotropic component of the EGRB is well below the reported limits.

~ 2 correction under reasonable assumptions, though the full impact of the updated instrument response functions (IRFs) requires a full reproduction of the analysis in Ackermann et al. (2012a). When coupled with the cosmic variance, this can boost the reported anisotropy to the minimum limits implied by the 2FGL. However, it is unable to increase it to the values suggested by smooth extrapolations of the 2FGL population to significantly lower fluxes.

Finally, the independence of the multipoles of the power spectrum of the masked gamma-ray sky fails for a small number ($N \lesssim 100$) of weak sources that dominate the anisotropy power spectrum. As shown in Appendix C.2, the covariance between different multipoles induces a floor on the statistical uncertainty comparable to that reported at high energies. In the case of the highest-energy bin, where the anisotropy is due entirely to the 21 unmasked sources in the 1FHL, the corresponding uncertainties are expected to be 10%–50% larger than those reported.

6. CONCLUSIONS

The contribution to the EGRB anisotropy arising from the now resolved point sources in the 2FGL and 1FHL detected above 5 GeV and lying outside of the mask employed by Ackermann et al. (2012a, which removed the galactic plane and all 1FGL point sources) is sufficient to fully explain the reported values at these energies, where BL Lac objects dominate the resolved extragalactic gamma-ray sky and the EGRB anisotropy has proved most constraining. This would imply that there cannot be any significant contribution from sources that fall just below the 2FGL and 1FHL detection thresholds, a conclusion belied by the absence of any evidence of spectral evolution with source flux. Thus, the unmasked 1FHL and 2FGL sources are in tension with the reported values of the anisotropy based on removing the 1FGL point sources.

Estimates of the EGRB anisotropy which employ the full 2FGL, extrapolating the flux contributions at all energy ranges via an empirically vetted band correction, significantly exceed the reported 1FGL-based measurements above 5 GeV. This represents a purely empirical estimate of the anisotropy associated with the known point-source population. In particular, we do not appeal to a parameterized source distribution, and hence our estimate represents a conservative lower limit on the EGRB anisotropy. Given that the 2FGL and the EGRB anisotropy observations are largely coincident, reconciling the apparent disparity between the estimates presented here and those reported in Ackermann et al. (2012a) is difficult. For estimates that make reasonable assumptions regarding the high-energy fluxes of 2FGL sources, the discrepancy above 10.4 GeV ranges from 2.6σ (direct) to 5.2σ (statistical, no Edington bias), with the 2FGL contribution alone exceeding that reported in Ackermann et al. (2012a) by a factor of 2.6–4.6, respectively.

The 2FGL limits are quite robust, independent of many of the complications that plague estimating the EGRB anisotropy directly⁸. In particular, it is insensitive to the particulars of the low-flux source population (which can only increase the anisotropy), and the dominant remaining source of potential uncertainty, cosmic variance, is small in comparison to the uncertainties on the reported anisotropy values. Given the lack of a precipitous decline in the number of sources immediately

below the 1FGL threshold observed in the 2FGL, and more recently, in the 1FHL below the 2FGL threshold, the observed discrepancy is unsurprising; the 2FGL overproduces the EGRB anisotropy for precisely the same reason that models of the gamma-ray point-source distributions do.

The limited flux range below the 1FGL threshold probed by the 2FGL implies that extrapolations of the 2FGL population to fluxes below the 2FGL threshold exceed the 2FGL limits by a substantial amount. Barring a cutoff immediately below the 2FGL limit, our estimates of the point-source contribution to the EGRB is an underestimate by at least a factor of two at high energies. As a consequence of the 2FGL detection threshold the 2FGL contribution to the EGRB anisotropy primarily probes the nearby AGN population (see Figure 36 of Ackermann et al. 2011). That is, unlike the EGRB anisotropy, generally, it does not provide an independent measure of the high-redshift AGN distribution. Thus, it is not surprising that models that reproduce the characteristics of the 2FGL are consistent with our implied limits upon the EGRB anisotropy (e.g., Broderick et al. 2014). Similarly, in the absence of a better understanding of the discrepancy between estimates of the EGRB anisotropy at high energies, as derived here from considering 2FGL and 1FHL sources versus those in Ackermann et al. (2012a) from the masked 1FGL, it is unclear if they provide an independent constraint on the high-redshift gamma-ray universe at present.

APPENDIX

A. ENERGY BAND AND SPECTRAL SHAPE CORRECTIONS

Computing the flux within the specific energy bands relevant for comparison to the measured EGRB anisotropy generally requires some spectral correction from fluxes measured in bands for which data is readily available. This depends on the spectral shape. We implement a band correction in two steps:

1. Considering only sources that are well fit by a power-law spectrum, we make a gross band correction for each object. With these, we construct the anisotropy spectrum.
2. We correct the above C_P for the observed spectral softening using a shape correction factor estimated by comparing the band-corrected fluxes to measured band-specific fluxes.

We describe each in detail here.

A.1. Band-correcting C_P using Power-law Spectra

The first band correction employs Equation (8) to construct the band-specific fluxes from the 1 GeV–100 GeV fluxes, i.e.,

$$\mathcal{F}_j = K(\Gamma_j) \mathcal{F}_{35,j} \quad \text{where} \quad K(\Gamma) \equiv \frac{E_m^{1-\Gamma} - E_M^{1-\Gamma}}{1 - 100^{1-\Gamma}}, \quad (\text{A1})$$

where $E_{m,M}$ are the lower and upper energy limits of the band in GeV, and \mathcal{F}_{35} is our standard flux reference.

Note that while the above provides the band correction for *individual* sources, since their individual spectra differ it is not equivalent to a single band correction, evaluated at some effective spectral index. At high energies, the population near the 1FGL detection threshold is dominated by increasingly hard sources, imparting an energy dependence on the typical spectral index and generally enhancing the anisotropy (see, e.g., Section VI of Cuoco et al. 2012).

⁸ Of course, this comes at the price of resolving the background, and thus is not a reasonable alternative.

A.2. Spectral Shape Corrections

Applying the band correction described above assumes that the source spectra are well approximated by power laws. Despite their characterization as such at lower energies, it is not clear that at high energies that this remains the case. In particular, above 100 GeV, considerable softening is anticipated for sources with redshifts $\gtrsim 0.5$. Thus, prior to using the band correction, here we assess its applicability and estimate the relevant spectral corrections. We do this by comparing the band-corrected \mathcal{F}_{35} to the fluxes measured in individual energy bands near those of interest.

For this purpose, we make use of both the 2FGL and 1FHL catalogs. Because of its longer duration and focus on sources above 10 GeV, the 1FHL affords better energy resolution and thus we ultimately make our correction based upon the subset of objects that appear in both the 1FHL and 2FGL. Nevertheless, to assess the impact of potential biases resulting from the 2FGL detection threshold, we also consider 2FGL sources alone. To exclude any putative Galactic component, we impose a cut on Galactic latitude of $|b| > 30^\circ$.

In both cases, the measured and band-corrected \mathcal{F}_{35} are clearly strongly correlated, exhibiting larger scatter at low fluxes, eventually developing a plateau, typically dominated by upper limits (see the right-hand panels of Figures 10 and 11). Importantly, the detection upper limits (absent at high energies in Figure 10 due to the definition of the 1FHL) plateau at measured fluxes *above* the band-corrected values. This implies that for the power-law sources we consider, there is no evidence for a flux-dependent evolution in the spectral shapes, i.e., sources near the detection threshold are spectrally similar to those above.

To avoid any potential Eddington bias in our estimated shape correction at low measured fluxes induced by the detection threshold, we institute a lower flux limit of the form

$$\mathcal{F}_{mM} \times (K\mathcal{F}_{35}) > \mathcal{F}_{\min}^2, \quad (\text{A2})$$

where \mathcal{F}_{\min} is an energy-band-dependent flux limit. The excluded region is denoted by the shaded regions in the right-hand panels of Figures 10 and 11, and the boundary is orthogonal to the expected proportionality relation (and therefore should not induce any Eddington bias). Values for the band-specific \mathcal{F}_{\min} adopted here are listed in Table 2.

We define the source-specific spectral correction by

$$k \equiv \frac{\mathcal{F}_{mM}}{K\mathcal{F}_{35}}, \quad (\text{A3})$$

which is simply the multiplicative correction to the band correction. Within each energy band, the distribution of k , shown in Figures 10 and 11, is well approximated by a log-normal distribution. The parameters of the distributions are relatively independent of the particular value of \mathcal{F}_{\min} employed. However, among bands, the distributions vary substantially. In the characterization of the properties of the k distributions, we have excluded outliers, which we define as objects with spectral corrections located more than three standard deviations from the mean. This has the effect of reducing the width of the distributions and biasing our estimated corrections to the EGRB anisotropy spectrum toward lower values, making it a conservative assumption.

At energies less than 30 GeV, the band-corrected fluxes are quite accurate, with mean spectral corrections, $\langle k \rangle$, all of the or-

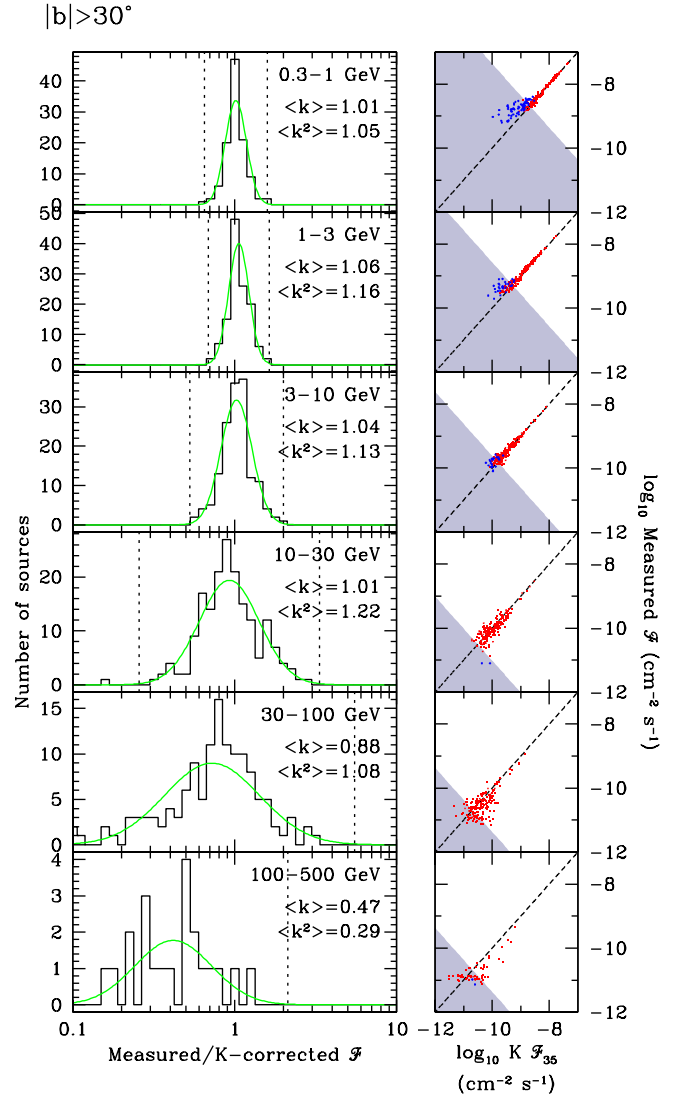


Figure 10. Left: distribution of the spectral shape corrections to the band-corrected \mathcal{F}_{35} for sources in the 1FHL and 2FGL catalogs for various energy bands. The green line shows a log-normal distribution fit. Sources beyond the vertical dashed lines are excluded so as not to bias the width toward larger values. Right: measured vs. only band-corrected \mathcal{F}_{35} within each energy band. Red and blue dots denote detections and upper limits, respectively. The dotted line shows the equal case, and the shaded area corresponds to the region excluded by Equation (A2).

der of unity for both the 1FHL and 2FGL samples.⁹ At high energies, $\langle k \rangle$ is less than unity, indicating the anticipated softening of the spectra. Moreover, there is some tentative evidence that this softening becomes more severe at higher energies.

However, since it is \mathcal{F}^2 that enters into the estimate of C_p employed here, of more importance is the mean-square spectral correction, i.e., $\langle k^2 \rangle$. This is impacted not only by the movement in the centroid of the k distribution but also by its width. Because of this, $\langle k^2 \rangle$ is larger than unity for all but the highest-energy bin and, by definition, is larger than $\langle k \rangle^2$. For the 30–100 GeV bin this is despite $\langle k \rangle \simeq 0.88$. The estimates of $\langle k^2 \rangle$ vary by about 1.13.

⁹ Note that $\log_{10} \langle k \rangle = \mu_k + 0.5\sigma_k^2 \ln 10$ for a log-normal distribution with $\mu_k \equiv \langle \log_{10} k \rangle$ and $\sigma_k^2 = \langle (\log_{10} k - \mu_k)^2 \rangle$. It is for this reason that $\langle k \rangle$ typically exceeds the mode in the distributions in Figures 10 and 11.

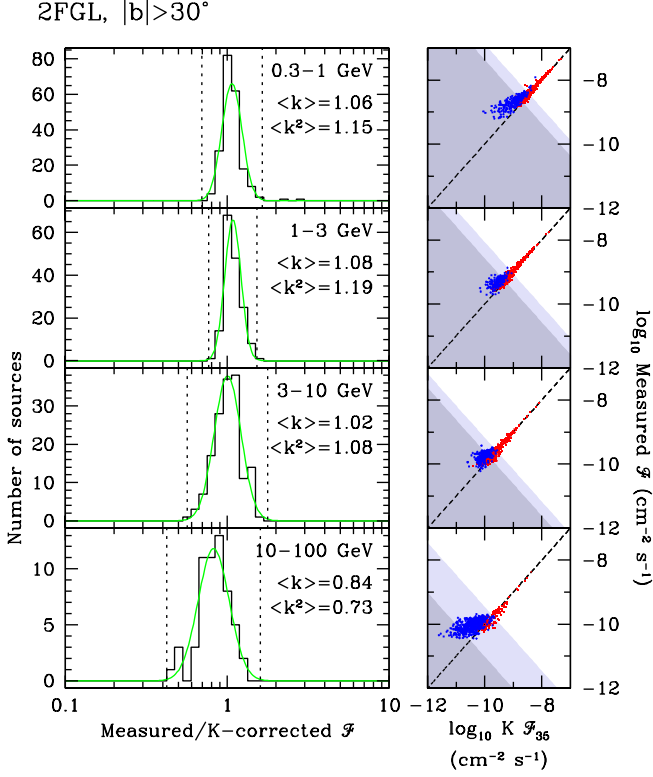


Figure 11. Left: distribution of the spectral corrections to the band-corrected \mathcal{F}_{35} for all power-law sources in the 2FGL catalog for various energy bands. The green line shows a log-normal distribution fit. Sources beyond the vertical dashed lines are excluded so as not to bias the width toward larger values. Right: measured vs. only band-corrected \mathcal{F}_{35} within each energy band. Red and blue dots denote detections and upper limits, respectively. The dotted line shows the equal case, and the light and dark gray shaded area corresponds to the region excluded by Equation (A2) for the 2FGL and 1FHL detection thresholds, respectively. Note that all of the upper limits (blue points) lie to the left of the trends associated with the detections (red points), implying that the detection upper limits lie above the band correction estimates. Thus, there is no evidence of a population of misidentified soft sources at high energies.

Repeating the above analysis with various other latitude cuts (e.g., $|b| > 20^\circ$, $|b| > 40^\circ$) yields nearly identical results, implying that the spectral corrections are indeed intrinsic to the extragalactic source population and are not associated with any contaminating Galactic subpopulation. Therefore, assuming that the distribution in k is uncorrelated with Γ or \mathcal{F}_{35} , we adopt a uniform spectral correction of 1.13 below 100 GeV, corresponding to the average value across bins at these energies.

B. C_P LIMIT ESTIMATE UNCERTAINTIES

B.1. Flux Reconstruction Errors on C_P

Uncertainty in the intrinsic 1 GeV–100 GeV fluxes and the spectral indexes produce a corresponding uncertainty in the band-corrected fluxes in the normal way and thus the estimated anisotropy. Here, we collect the relevant error propagation formula and some comments on its magnitude. Because of its weak energy dependence, we will neglect the impact of the spectral shape correction, focusing entirely on the impact of the power-law band correction.

Assuming no correlation in the errors on \mathcal{F}_{35} and Γ , we have an uncertainty in the power law band corrected flux of

$$\frac{\sigma_{\mathcal{F}_j}^2}{\mathcal{F}_j^2} = \frac{\sigma_{\mathcal{F}}^2}{\mathcal{F}_{35}^2} + \frac{\sigma_K^2}{K^2}, \quad (\text{B1})$$

Table 4
Kolmogorov-Smirnov
Comparison of Latitude
Cuts

b_{\min}	$P_{\text{KS}}^{\mathcal{F}_{35}}$	P_{KS}^{Γ}
0°	9.2×10^{-6}	0.13
5°	3.2×10^{-4}	0.43
10°	9.7×10^{-3}	0.65
15°	0.15	0.70
20°	0.60	0.74
25°	0.97	1.0
30°	1.0	1.0
35°	0.96	1.0
40°	0.30	0.98
45°	0.23	0.48

where

$$\frac{\sigma_K}{K} = \left| \frac{\ln(E_m)E_m^{1-\Gamma} - \ln(E_M)E_M^{1-\Gamma}}{E_m^{1-\Gamma} - E_M^{1-\Gamma}} - \frac{\ln(1) - \ln(100)100^{1-\Gamma}}{1 - 100^{1-\Gamma}} \right| \sigma_\Gamma, \quad (\text{B2})$$

in which $E_{m,M}$ are the energies bounding the desired band. Note that as expected when $E_{m,M}$ approaches 1 GeV–100 GeV the σ_K term vanishes, and the band-corrected flux uncertainty reduces to that associated with the intrinsic flux uncertainty.

To obtain the associated uncertainty in the anisotropy, we make the further assumption that the flux uncertainties among sources are uncorrelated, and thus

$$\frac{\sigma_{C_P}^2}{C_P^2} = \sum_j (2w_j \mathcal{F}_j)^2 \sigma_{\mathcal{F}_j}^2 / \left(\sum_j w_j \mathcal{F}_j^2 \right)^2. \quad (\text{B3})$$

This ranges from 2% at low energies to 7% at high energies, and in all cases, is smaller than that implied by the cosmic variance (see the following section).

The fractional errors in C_P may appear unexpectedly low given the typical fractional flux errors of 15%–25% near the flux threshold. However, the reason for this is simply that the C_P is essentially an average over \mathcal{F}_j^2 . That is, for a population of N sources with identical fluxes at the threshold, this is roughly

$$\frac{\sigma_{C_P}^2}{C_P^2} \simeq \frac{4\mathcal{F}_j^2 \sigma_{\mathcal{F}_j}^2 N}{\mathcal{F}_j^4 N^2} \simeq \frac{4}{N} \frac{\sigma_{\mathcal{F}_j}^2}{\mathcal{F}_j^2}. \quad (\text{B4})$$

Hence, for $N \simeq 10$ sources near the threshold and $\sigma_{\mathcal{F}_j}/\mathcal{F}_j \simeq 0.25$, the anticipated fractional uncertainty in C_P arising from the flux uncertainty is 3%.

B.2. Cosmic Variance

Our method of summing over the unmasked 2FGL sources to obtain a lower limit on C_P (in either our conservative direct or statistical approaches) allows a less stringent latitude cut than that applied by the *Fermi*-LAT collaboration to increase the statistics of the source number. Of course, this is only justified if there is no contaminating Galactic population of point sources, which would bias the inferred values of C_P . Here, we demonstrate that this is indeed the case: above 15° the source populations are statistically indistinguishable from that above 30° . Following this, we estimate the cosmic variance in the measured C_P via the cumulative and differential contributions to the anisotropy from various Galactic latitude cuts.

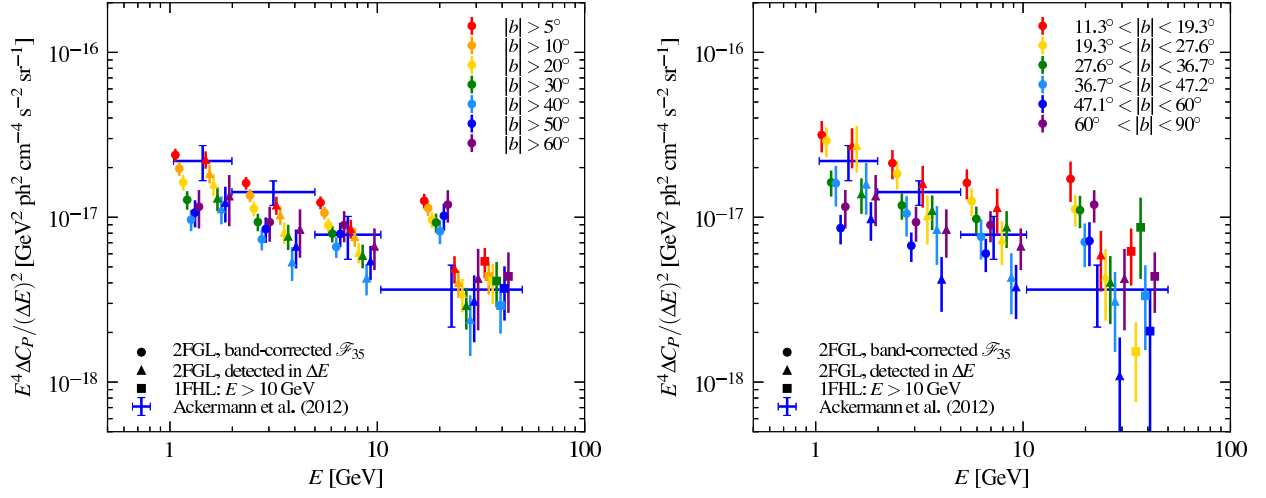


Figure 12. Contribution to the EGRB anisotropy ΔC_P by unmasked point sources. We contrast the cumulative (left) and differential (right) contribution of galactic latitude (color coded for different cuts). We compare the reported measurements of C_P (blue, Ackermann et al. 2012a) to the contribution of individual unmasked 2FGL sources, which are detected in the respective energy bins (triangles) and the unmasked 1FHL sources above 10 GeV (squares). We show the contribution of all unmasked 2FGL sources (detected above 1 GeV) that are band corrected to the respective energy band (circles). The error bars account for cosmic variance, and the data points have been shifted horizontally within their respective energy bin centers for clarity.

B.2.1. Excluding the Galactic Point-source Population

Extending the 2FGL to lower latitudes than the 30° cut made by Ackermann et al. (2012a) results in a considerably larger sample size and correspondingly lower cosmic variance. Moreover, it provides additional realizations with which to estimate the cosmic variance expected for the measured anisotropy spectrum. Here, we verify that less stringent latitude cuts are allowed by the 2FGL (though perhaps not by the diffuse Galactic emission) by comparing the distribution of source properties at different latitudes via the Kolmogorov-Smirnov (K-S) test.

Since the K-S test is one-dimensional, we explicitly compare the source flux (\mathcal{F}_{35}) distribution and photon spectra index (Γ) distribution separately. A cursory comparison by eye of the joint distribution does not reveal any noticeable correlation, suggesting that the comparison of the projected distributions is sufficient.

The K-S test returns a probability that may be loosely interpreted as the likelihood that two samples drawn from the same distribution differ as much as the two being compared. These are listed for a variety of latitude cuts, encompassing the 30° employed by Ackermann et al. (2012a), for the flux and photon spectral index distributions in Table 4. (The inclusion of $b_{\min} = 30^\circ$ is gratuitous and returns the expected probability of unity.) In these, very small values indicate differing source populations. Fluctuations become large at very high latitude cuts due to the small number of remaining sources. However, at latitudes below 15° , the disparity can only be explained by the presence of an additional, Galactic population. Above latitudes of 20° , this population is subdominant, and above 25° it may be ignored altogether. These correspond to an increase of nearly 31% and 14% in the total source count, respectively.

B.2.2. Direct Estimates of the EGRB Anisotropy for Varying Galactic Latitude

In Figure 12, we show the cumulative and differential contribution to the EGRB anisotropy ΔC_P by unmasked point sources for varying galactic latitude. We perform a Monte Carlo integration of the sky coverage after applying the respective masks to obtain the unmasked sky frac-

tions $f_{\text{sky}} = \{0.613, 0.556, 0.446, 0.338, 0.240, 0.158, 0.093\}$ for $|b| > \{5^\circ, 10^\circ, 20^\circ, 30^\circ, 40^\circ, 50^\circ, 60^\circ\}$ (a similar computation using the 2FGL to construct the mask yields $f_{\text{sky}}^{2\text{FGL}} = \{0.556, 0.507, 0.406, 0.310, 0.222, 0.145, 0.083\}$ for the same latitude cuts). For the differential ΔC_P , our Monte Carlo integration in galactic area rings of equal area (indicated in Figure 12) yield sky fractions that scatter around 0.09.

At low energies, there is a systematic trend of an increasing cumulative ΔC_P for decreasing galactic latitude, which could be due to two reasons: (1) since the different values for ΔC_P are not statistically independent (a less stringent galactic latitude cut contains the point sources with a more conservative cut as a subsample), this sequence of ΔC_P could be due to a regression to a (high) mean with increasing sample size, or (2) this could sign a population of soft-spectrum galactic point sources out to $|b| < 30^\circ$. At energies $E > 10$ GeV, the differential contribution to C_P of equal-sky-area galactic latitude rings shows no systematic trend in the (more complete) 1FHL sample and in the 2FGL sample for $|b| > 20^\circ$. The data are inconclusive whether the low-energy data points at $|b| < 30^\circ$ signal positive outliers or the hint of a population of soft-spectrum galactic point sources. Our K-S test suggests the first possibility and that it is safer to use point sources with $|b| > 20^\circ$ (at least at higher energies).

C. POSSIBLE SOURCES OF REPORTED ANISOTROPY DISCREPANCY

Here, we collect some illustrative computations that may explain the discrepancy between the high-energy anisotropy reported by Ackermann et al. (2012a) and the limits implied by this analysis. We do not make any claims regarding completeness, restricting ourselves to exploring plausibility. These take two forms: modifications of the PSF, which shift the expected measured value upward, and additional sources of uncertainty, which lessen the statistical significance of the discrepancy.

C.1. Fermi Point-spread Function

We begin with a gross estimate of the impact of the recent update of the PSF on the deconvolution procedure employed

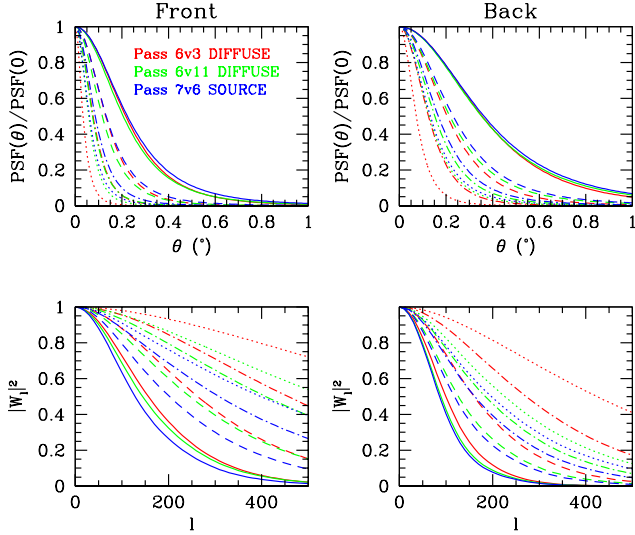


Figure 13. Point-functions (top) for the front (left) and back (right) LAT detectors for the energy bands relevant for the EGRB anisotropy measurements for the Pass 6v3 DIFFUSE (red), Pass 6v11 DIFFUSE (green), and Pass 7v6 SOURCE (blue) IRFs, and their associated window functions (bottom). The point-spread function/window function for the 1.04–1.99 GeV, 1.99–5.00 GeV, 5.00–10.4 GeV, and 10.4–50.0 GeV energy bands are shown by the solid, long-dash, short-dash, and dotted lines, respectively. Varying the Pass 7v6 event class makes only a marginal difference. Binning the PSF on the scales implied in Ackermann et al. (2012a) reduces the $|W_\ell|^2$ for the highest-energy bin, though it does so roughly in proportion for both IRFs.

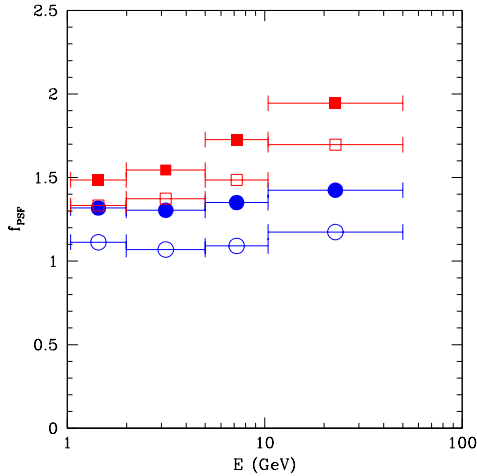


Figure 14. Correction factor relating the EGRB anisotropy spectrum using the Pass 6v3 DIFFUSE and Pass 6v11 DIFFUSE IRF (open) and the Pass 6v3 DIFFUSE and Pass 7v6 SOURCE IRF (filled) to deconvolve the beam. The correction for the front and back detector in the LAT are shown by the blue circles and red squares, respectively. Binning the PSF on the scales implied in Ackermann et al. (2012a) and considering alternative Pass 7v6 event classes have only a marginal impact.

by Ackermann et al. (2012a). The PSF used was from the Pass 6v3 DIFFUSE IRF, and based on erroneous Monte Carlo simulations of the detector. However, comparisons of the apparent structure of bright, compact Galactic and extragalactic

sources conclusively demonstrated that the Pass 6v3 PSF must be considerably broader than originally stated (Neronov et al. 2011). Correspondingly, subsequent on-orbit calibrations, first reported in Pass 6v11 IRF and used above 1 GeV in the current IRF, Pass 7v6, exhibit much broader PSFs at high energies for all event classes and are consistent with those found in (Neronov et al. 2011). Here, we employ both the updated Pass 7v6 and the Pass 6v11 DIFFUSE PSFs as proxies for the true PSF to assess the potential magnitude of the correction this implies. Note that this is similar in principle to the comparison made in Section D of Ackermann et al. (2012a), though even a cursory consideration of the PSFs shown in Ackermann et al. (2012b) would seem to call into question the remarkable agreement between the Pass 6v3 and Pass 6v11 results found in Ackermann et al. (2012a) at the highest energies.

Different IRF versions potentially place different intrinsic cuts on individual event properties and thus may include different event lists, complicating any direct comparison. This is exacerbated by changes in the stated event classes among subsequent IRF releases. While Ackermann et al. (2012a) utilized the Pass 6v3 DIFFUSE class events, no such event class exists in the Pass 7 IRFs. Here, we discuss the comparison with the Pass 7v6 SOURCE events, chosen as superficially the most comparable based upon their description and following the comparisons made in Section 6.6 of Ackermann et al. (2012b). However, considering the Pass 7v6 CLEAN IRFs as a proxy instead results in only marginal differences.

Despite the uncertainty in the event lists, it is clear that above 1 GeV, the evolution in the IRFs between Pass 6v3, Pass 6v11, and Pass 7v6 is dominated by the differences in the PSF estimation scheme and not the intrinsic event reconstruction (Ackermann et al. 2012b). Thus, we expect that the magnitude of the impact of the PSF on the resulting anisotropy spectrum is well approximated by the comparison between the Pass 6v3 DIFFUSE, Pass 6v11 DIFFUSE, and Pass 7v6 SOURCE PSFs. Differences due to the lack of the tail term in the Pass 7 PSF parameterization will only increase the disparity.

The PSF impacts the anisotropy measurement through the window function, employed in the beam deconvolution and defined by

$$W_\ell = 2\pi \int_{-1}^1 d\mu P_\ell(\mu) \text{PSF}(\theta), \quad (\text{C1})$$

where $\mu \equiv \cos \theta$ and P_ℓ are Legendre polynomials. The Pass 6v3 DIFFUSE, Pass 6v11 DIFFUSE, and Pass 7v6 SOURCE PSFs and window functions in the energy bands of interest, assuming a spectral index of $\Gamma = 2.2$, are compared in Figure 13. These may be compared with the window functions shown in Figure 9 of Ackermann et al. (2012a), and indirectly with Figure 65 of Ackermann et al. (2012b). Since the PSF deconvolved anisotropy signal is $\propto |W_\ell|^{-2}$ (see Equation (4) of Ackermann et al. 2012a), underestimating the width of the PSF (and thus overestimating $|W_\ell|^2$) results in an associated underestimate of the anisotropy.

The magnitude of the correction to the window function depends on the multipole at which the C_ℓ is determined. Assuming that the estimate of C_P arises from a least squares fit of a constant to the observed C_ℓ for $150 \leq \ell \leq 500$ and that the uncertainty in the power spectrum prior to deconvolution is dominated by photon shot noise at low ℓ , the relevant correction

is

$$f_{\text{PSF}}^V = \left[\frac{\sum_{\ell} (2\ell+1) |W_{\ell}^V|^2}{\sum_{\ell} (2\ell+1) |W_{\ell}^V|^4} \right] / \left[\frac{\sum_{\ell} (2\ell+1) |W_{\ell}^{6v3}|^2}{\sum_{\ell} (2\ell+1) |W_{\ell}^{6v3}|^4} \right], \quad (\text{C2})$$

which receives substantial contributions from large ℓ . This is shown for both the back and front detectors in Figure 14, with a typical value at high energies ranging from 1.2 to 2.0.

In practice, the correction factor depends upon the fraction of the anisotropy signal associated with the front and back detectors. Given the similarity in the effective area of the two LAT detectors, adopting an equal anisotropy signal in each gives an effective correction factor of roughly 1.6. Furthermore, the anisotropy estimates in Ackermann et al. (2012a) were obtained via the variance weighted means of an estimate of the power spectrum separate from front- and back-converted events, and thus, the back detector and regions with large uncertainties are expected to contribute less to the resulting anisotropy value. However, at high energies, where the discrepancies reported here are largest, the uncertainties are essentially independent of multipole for $\ell \geq 150$ and similar for the front and back detector, reducing the impact of the variance weighting (see Section III.C of Ackermann et al. 2012a).

C.2. C_P Variance in the Few Photon Limit

The anisotropy spectrum derived in Ackermann et al. (2012a) employed analyses derived originally for the cosmic microwave background (e.g., Knox 1995), corresponding to the limit of small fluctuations and large numbers of photons. However, the statistics of power spectrum reconstruction from a small population of dim point sources differs significantly from that associated with many photons continuously distributed throughout the sky. Most importantly, in the former case, *source* shot noise, similar to the frequently discussed photon shot noise, effectively limits the independence of multipoles in the power spectrum, and thus the variance of any reconstruction of C_P . Here, we present an illustrative computation of the variance associated with estimates of C_P arising from a population of identical point sources, computed by averaging the power spectrum over a range in multipoles, similar in spirit to the measurement by Ackermann et al. (2012a).

The estimate of C_P presented in Ackermann et al. (2012a) is constructed in a number of steps, beginning with the measurement of the C_{ℓ}^{raw} from the intensity sky maps. From these, after correcting for the sky coverage, the photon shot noise is removed and the PSF deconvolved, resulting in

$$C_{\ell}^{\text{signal}} = \frac{C_{\ell}^{\text{raw}} / f_{\text{sky}} - C_N}{|W_{\ell}|^2} \quad (\text{C3})$$

where C_N is the average number of photons in a given sky pixel and represents the photon shot noise term (see Equation (4) of Ackermann et al. 2012a). The C_{ℓ}^{signal} are then averaged over 50 multipole bins, producing an estimate of the power spectrum. Finally, the variance weighted mean of the power spectrum provides the desired value of C_P (Equation (8) of Ackermann et al. 2012a).

Here, we will make a variety of simplifying assumptions in the interest of clarity.¹⁰ The first is that we may ignore

¹⁰ Relaxing any of these assumptions, the most important of which is the uniformity of the source fluxes, only increases the size of the corresponding source shot noise. This is because doing so generally decreases the number of effective objects that dominate the statistics of the power spectrum reconstruction.

the complications induced by the limited sky coverage, i.e., $f_{\text{sky}} = 1$. The second is that the beam width is much smaller than the scales of interest and thus $|W_{\ell}|^2 \approx 1$. Together, these give $C_{\ell}^{\text{signal}} = C_{\ell}^{\text{raw}} - C_N$. Third, we will assume that the noise in the reconstructed power spectrum is roughly independent of multipole (ℓ and m). This is not strictly the case above 5 GeV in Ackermann et al. (2012a) (see, e.g., Figure 3), for which the variance as a function of multipole appears nearly constant because of the suppression due to the window function. However, the limited range of multipoles implies that this will make at most a factor of a few change to the variance estimates obtained here, with the true values being somewhat larger. With this assumption, the photon-shot-noise variance weighted mean of the power spectrum, the estimate of the anisotropy employed in Ackermann et al. (2012a), corresponds to an unweighted average over all multipoles. Fourth, we will ignore any intrinsic source structure. As a result, the variance weighted mean approximately becomes an unweighted average, and the averaging within and across bins may be done in a single step. Therefore, the estimator we consider is

$$C_P = \frac{\sum_{\ell=\ell_{\min}}^{\ell_{\max}} (C_{\ell}^{\text{raw}} - C_N) / \sigma_n^2}{\sum_{\ell=\ell_{\min}}^{\ell_{\max}} 1 / \sigma_n^2} \approx \frac{1}{L} \sum_{\ell,m} C_{\ell,m}^{\text{raw}} - C_N, \quad (\text{C4})$$

where we have suppressed the summation limits for compactness, $L \equiv (\ell_{\max} + 1)^2 - (\ell_{\min} + 1)^2$ is the total number of multipoles included, $\sigma_n^2 \propto (2\ell + 1)^{-1}$ is the variance due to photon shot noise alone (the only source of noise employed by Ackermann et al. 2012a), and ℓ_{\min} and ℓ_{\max} are the minimum and maximum multipoles considered. Finally, we will assume a uniform observing time across the entire sky, Δt , in terms of which

$$C_N = \frac{n}{\Delta t^2}, \quad (\text{C5})$$

where n is the total number of events observed.

For a population of point sources, the power spectrum in the flat-sky approximation (which is valid for $\ell_{\min} \gtrsim 15$ for the point-source samples considered in this work) is given by

$$C_{\ell,m}^{\text{raw}} = \frac{1}{\Delta t^2} \sum_{a,b=1}^N M_a M_b e^{i\ell \cdot (\mathbf{x}_a - \mathbf{x}_b)}, \quad (\text{C6})$$

where $M_{a,b}$ are Poisson deviates with mean \bar{M}_a corresponding to the expected number of photons during the entire observation for each source, and $\mathbf{x}_{a,b}$ are the positions of the sources on the sky. The corresponding C_P estimate, obtained by inserting this into Equation (C4), is then

$$C_P = \frac{1}{\Delta t^2} \left[\frac{1}{L} \sum_{\ell,m} \sum_{a,b} M_a M_b e^{i\ell \cdot (\mathbf{x}_a - \mathbf{x}_b)} - \sum_a M_a \right]. \quad (\text{C7})$$

The mean C_P is obtained by averaging over source realizations, i.e., both M and \mathbf{x} , which are presumed to be uncorrelated:

$$\begin{aligned} \langle C_P \rangle &= \frac{1}{\Delta t^2} \left\{ \frac{1}{L} \sum_{\ell,m} \left[\sum_a \langle M_a^2 \rangle + \sum_{a \neq b} \langle M_a M_b e^{i\ell \cdot (\mathbf{x}_a - \mathbf{x}_b)} \rangle \right] - \sum_a \langle M_a \rangle \right\} \\ &= \frac{1}{\Delta t^2} \sum_a [\langle M_a^2 \rangle - \langle M_a \rangle] = \frac{1}{\Delta t^2} \sum_a \bar{M}_a^2 \end{aligned} \quad (\text{C8})$$

Note this is precisely the value anticipated by Equation (6).

The variance in this C_P estimate is given by

$$\begin{aligned}
 \sigma_{C_P}^2 &= \langle C_P^2 \rangle - \langle C_P \rangle^2 \\
 &= \frac{1}{\Delta t^4} \left\{ \frac{1}{L^2} \left\langle \sum_{\ell, m, \ell', m'} \sum_{a, b, c, d} M_a M_b M_c M_d e^{i\ell \cdot (\mathbf{x}_a - \mathbf{x}_b) + i\ell' \cdot (\mathbf{x}_c - \mathbf{x}_d)} \right\rangle \right. \\
 &\quad \left. - \frac{2}{L} \left\langle \sum_{\ell} \sum_{a, b, c} M_a M_b M_c e^{i\ell \cdot (\mathbf{x}_a - \mathbf{x}_b)} \right\rangle \right. \\
 &\quad \left. + \left\langle \sum_{a, b} M_a M_b \right\rangle - \left(\sum_a \bar{M}_a^2 \right)^2 \right\} \\
 &= \frac{1}{\Delta t^4} \left\{ \frac{1}{L^2} \left[\sum_{(\ell, m) \neq (\ell', m')} \left\langle \sum_a M_a^4 + \sum_{a \neq b} M_a^2 M_b^2 \right\rangle \right. \right. \\
 &\quad \left. + \sum_{\ell, m} \left\langle \sum_a M_a^4 + 2 \sum_{a \neq b} M_a^2 M_b^2 \right\rangle \right] \\
 &\quad - \frac{2}{L} \sum_{\ell, m} \left\langle \sum_a M_a^3 + \sum_{a \neq b} M_a M_b^2 \right\rangle \\
 &\quad \left. + \left\langle \sum_a M_a^2 + \sum_{a \neq b} M_a M_b \right\rangle - \left(\sum_a \bar{M}_a^2 \right)^2 \right\}. \tag{C9}
 \end{aligned}$$

After inserting the appropriate moments of the Poisson distribution this simplifies to

$$\sigma_{C_P}^2 = \frac{1}{\Delta t^4} \left[\sum_a 2\bar{M}_a^2 (2\bar{M}_a + 1) + \frac{2}{L} \sum_{a \neq b} \bar{M}_a (\bar{M}_a + 1) \bar{M}_b (\bar{M}_b + 1) \right]. \tag{C10}$$

In addition to the extragalactic sources of primary interest here, the background also consists of a dominant diffuse galactic component. Above $\ell_{\min} \approx 100$, the diffuse component does not contribute to C_P significantly, though it continues to dominate $\sigma_{C_P}^2$. Within the context of the above formalism, we imagine the background as due to a population of N sources with equal flux such that $\bar{M} \gtrsim 1$, and $N_G \gg N$ galactic sources with equal flux $\bar{M}_G \ll 1$, in terms of which

$$C_P = \frac{1}{\Delta t^2} (N\bar{M}^2 + N_G\bar{M}_G^2) = \frac{1}{\Delta t^2} \left(N\bar{M}^2 + \frac{n_G^2}{N_G} \right) \tag{C11}$$

and

$$\begin{aligned}
 \sigma_{C_P}^2 &\approx \frac{1}{\Delta t^4} \left[4N\bar{M}^3 + 2N_G\bar{M}_G^2 + \frac{2}{L} (N^2\bar{M}^4 + N_G^2\bar{M}_G^2) \right] \\
 &\approx \frac{1}{\Delta t^4} \left[4N\bar{M}^3 + \frac{2n_G^2}{N_G} + \frac{2}{L} (N^2\bar{M}^4 + n_G^2) \right], \tag{C12}
 \end{aligned}$$

where $n_G \equiv N_G\bar{M}_G \gg n$, $n_G \gg C_P\Delta t^2$, in which $n \equiv N\bar{M}$. In the smooth limit for the diffuse Galactic component $N_G \rightarrow \infty$ while n_G is fixed, and thus after some simplification, the limiting expressions are

$$C_P \approx \frac{1}{\Delta t^2} N\bar{M}^2 \quad \text{and} \quad \sigma_{C_P}^2 \approx \frac{4}{n} C_P^2 + \frac{2}{L} \frac{n_G^2}{\Delta t^4}. \tag{C13}$$

The second term decreases linearly with $1/L$, i.e., as expected for an average of independent multipoles. However, the former term is fixed and arises due to the correlations induced among photons resulting from having come from a fixed number of potential sources. This source shot noise term, analogous to the photon shot noise, dominates when

$$L \gtrsim \frac{nn_G^2}{2C_P^2\Delta t^4}. \tag{C14}$$

In the case of interest, roughly $N = 21$ sources within the 1FHL are capable of completely reproducing the anisotropy above 10.4 GeV, with an average flux of

$$\bar{F} = \sqrt{\frac{C_P}{N/(4\pi f_{\text{sky}})}} \simeq 6.5 \times 10^{-11} \text{ ph cm}^{-2} \text{ s}^{-1}, \tag{C15}$$

where we adopted $f_{\text{sky}} = 0.338$ (see Appendix B.2.2). Assuming a field of view of $\Omega_{\text{fov}} = 2.4$ sr, effective area of $A_{\text{eff}} = 7000 \text{ cm}^2$, and livetime of $\tau_1 = 56.6 \text{ Ms}$ (see Section II of Ackermann et al. 2012a), this translates into roughly

$$\bar{M} = \bar{F} \frac{\Omega_{\text{fov}}}{4\pi} A_{\text{eff}} \tau_1 \simeq 4.9, \tag{C16}$$

i.e., five photons per source, consistent with the reported sensitivity in Section 2.3 of Ackermann et al. (2013). Thus, the source shot noise effectively places a floor of 20% on the fractional error in the reconstructed value of C_P . This is roughly half as large as the reported errors above 10.4 GeV, suggesting that at most this modifies the uncertainty estimates by 10%–50%.

The authors thank Niayesh Afshordi, Alessandro Cuoco, Jennifer Siegal-Gaskins, and the *Fermi* collaboration for helpful discussions and Volker Springel for careful reading of the manuscript. A.E.B. and K.S. receive financial support from the Perimeter Institute for Theoretical Physics and the Natural Sciences and Engineering Research Council of Canada through a Discovery Grant. Research at Perimeter Institute is supported by the Government of Canada through Industry Canada and by the Province of Ontario through the Ministry of Research and Innovation. C.P. gratefully acknowledges financial support of the Klaus Tschira Foundation. E.P. acknowledges support by the DFG through Transregio 33. P.C. gratefully acknowledges support from the UWM Research Growth Initiative, from *Fermi* Cycle 5 through NASA grant NNX12AP24G, from the NASA ATP program through NASA grant NNX13AH43G, and NSF grant AST-1255469.

REFERENCES

- Abdo, A. A., Ackermann, M., Ajello, M., et al. 2010a, *ApJS*, 188, 405
- . 2010b, *ApJ*, 720, 435
- Ackermann, M., Ajello, M., Allafort, A., et al. 2011, *ApJ*, 743, 171
- . 2013, *ApJS*, 209, 34
- Ackermann, M., et al. 2012a, *Phys. Rev. D*, 85, 083007
- . 2012b, *ApJS*, 203, 4
- . 2012c, *Science*, 338, 1190
- Broderick, A. E., Chang, P., & Pfrommer, C. 2012, *ApJ*, 752, 22
- Broderick, A. E., Pfrommer, C., Puchwein, E., & Chang, P. 2014, *ApJ*, 790, 137
- Cavadini, M., Salvaterra, R., & Haardt, F. 2011, *arXiv:1105.4613*
- Cuoco, A., Komatsu, E., & Siegal-Gaskins, J. M. 2012, *Phys. Rev. D*, 86, 063004
- Domínguez, A., Finke, J. D., Prada, F., Primack, J. R., Kitaura, F. S., Siana, B., & Paneque, D. 2013, *ApJ*, 770, 77

- Eddington, A. S. 1913, MNRAS, 73, 359
Eddington, Sir, A. S. 1940, MNRAS, 100, 354
Harding, J. P., & Abazajian, K. N. 2012, JCAP, 11, 26
Knox, L. 1995, Phys. Rev. D, 52, 4307
Maccarone, T. J., Gallo, E., & Fender, R. 2003, MNRAS, 345, L19
McHardy, I. M., Koerding, E., Knigge, C., Uttley, P., & Fender, R. P. 2006, Nature, 444, 730
Neronov, A., Semikoz, D. V., Tinyakov, P. G., & Tkachev, I. I. 2011, A&A, 526, 90
Nolan, P. L., Abdo, A. A., Ackermann, M., et al. 2012, ApJS, 199, 31
Singal, J., Petrosian, V., & Ajello, M. 2012, ApJ, 753, 45
Wall, J. V., Jackson, C. A., Shaver, P. A., Hook, I. M., & Kellermann, K. I. 2005, A&A, 434, 133
Willott, C. J., Rawlings, S., Blundell, K. M., Lacy, M., & Eales, S. A. 2001, MNRAS, 322, 536